Monthly Notices
of the
ROYAL ASTRONOMICAL SOCIETY

MNRAS **429,** 3449–3471 (2013) doi:10.1093/mnras/sts611

Probing nuclear activity versus star formation at $z \sim 0.8$ using near-infrared multi-object spectroscopy

C. Ramos Almeida,[1,2]★ J. M. Rodríguez Espinosa,[1,2] J. A. Acosta-Pulido,[1,2] A. Alonso-Herrero,[3]† A. M. Pérez García[1,2] and N. Rodríguez-Eugenio[1,2]

[1]*Instituto de Astrofísica de Canarias (IAC), C/Vía Láctea, s/n, E-38205 La Laguna, Tenerife, Spain*
[2]*Departamento de Astrofísica, Universidad de La Laguna, E-38205 La Laguna, Tenerife, Spain*
[3]*Instituto de Física de Cantabria, CSIC-Universidad de Cantabria, E-39005 Santander, Spain*

Accepted 2012 December 12. Received 2012 December 12; in original form 2012 July 9

ABSTRACT

We present near-infrared (NIR) spectroscopic observations of 28 X-ray and mid-infrared selected sources at a median redshift of $z \sim 0.8$ in the Extended Groth Strip (EGS). To date this is the largest compilation of NIR spectra of active galactic nuclei (AGN) at this redshift. The data were obtained using the multi-object spectroscopic mode of the Long-slit Intermediate Resolution Infrared Spectrograph (LIRIS) at the 4.2 m William Herschel Telescope (WHT). These galaxies are representative of a larger sample studied in a previous work, consisting of over a hundred X-ray selected sources with mid-infrared counterparts, which were classified either as *AGN dominated* or *host galaxy dominated*, depending on the shape of their spectral energy distributions (SEDs). Here, we present new NIR spectra of 13 and 15 sources of each class, respectively. We detect the Hα line at $\geq 1.5\sigma$ above the continuum for the majority of the galaxies. Using attenuation-corrected Hα luminosities and observed *Spitzer*/MIPS 24 μm fluxes, and after subtracting an AGN component estimated using an AGN empirical correlation and multifrequency SED fits, we obtain average star formation rates (SFRs) of 7 ± 7 and 20 ± 50 $M_\odot$ yr^{-1}, respectively (median SFRs = 7 and 5 $M_\odot$ yr^{-1}). These values are lower than the SFRs reported in the literature for different samples of non-active star-forming galaxies of similar stellar masses and redshifts ($M_* \sim 10^{11}$ $M_\odot$ and $z \sim 1$). In spite of the small size of the sample studied here, as well as the uncertainty affecting the AGN-corrected SFRs, we speculate with the possibility of AGN quenching the star formation in galaxies at $z \sim 0.8$. Alternatively, we might be seeing a delay between the offset of the star formation and AGN activity, as observed in the local Universe.

Key words: galaxies: active – galaxies: nuclei – galaxies: star formation – infrared: galaxies.

1 INTRODUCTION

The role of active galactic nuclei (AGN) in the formation and evolution of galaxies is still not well established. It is not clear whether AGN represent episodic phenomena in the life of galaxies are random processes (given that the supermassive black hole (SMBH) is already there, at least in the local Universe), or are more fundamental. Some authors claim that AGN are key in quenching the star formation in their host galaxies through the so-called AGN feedback (see e.g. Granato et al. 2004; Ho 2005; Springel, Di Matteo & Hernquist 2005; Schawinski et al. 2007, 2009). This 'negative' AGN feedback has been invoked to explain the well-established correlations between SMBH mass and host galaxy properties (e.g. Kormendy & Richstone 1995; Magorrian et al. 1998; Ferrarese & Merritt 2000; Gebhardt et al. 2000; Greene & Ho 2006). A similar correlation has been observed in starburst galaxies, in which bright stellar clusters, also called central massive objects (CMO), take the role of the SMBH (Ferrarese et al. 2006; Wehner & Harris 2006).

In order to understand the importance of the AGN feedback in the evolution and the star formation histories of galaxies, it is necessary to study how the star formation rate (SFR) in active galaxies evolves with redshift. AGN at cosmological distances have been widely studied in the optical due to the relatively high number of multi-object spectrographs in this range. On the other hand, the sparse number of these instruments in the near-infrared (NIR) translates in the lack of spectroscopic studies of distant AGN in the NIR. This range offers the opportunity to study the optical spectra of galaxies at $z \sim 1$. At this redshift, the Hα line is shifted into the *J* band. This

★E-mail: cra@iac.es
† Augusto González Linares Senior Research Fellow

recombination line is a good tracer of the instantaneous SFR, since it is proportional to the ionizing ultraviolet (UV) Lyman continuum radiation from young and massive stars and it has little dependence on metallicity (Kennicutt 1998; Bicker & Fritze-v. Alvensleben 2005). Characterizing the SFRs of active galaxies using either Hα or any other indicator (e.g. the IR emission) is very challenging, as the AGN contributes to both the continuum and the emission line spectrum. Thus, estimates of the SFRs of powerful AGN, as for example quasars, will be contaminated with AGN emission to a certain extent. On the other hand, the SFRs of deeply buried and optically dull AGN obtained from Hα emission may only have a small contribution from the AGN. These optically dull AGN are defined as X-ray-selected AGN with no evidence for nuclear accretion activity in optical spectroscopy, showing stellar emission-dominated or obscured optical-to-infrared (IR) SEDs instead, practically indistinguishable from those of spiral/starburst galaxies (Alonso-Herrero et al. 2004, 2008; Rigby et al. 2006; Trump et al. 2009).

The star formation activity in the hosts of AGN at $z \sim 1$ has been studied by several authors using mid-infrared (MIR), far-infrared (FIR) and submillimetre data (Alonso-Herrero et al. 2008; Bundy et al. 2008; Brusa et al. 2009; Lutz et al. 2010; Santini et al. 2012). The latter authors found that the period of moderately luminous AGN activity does not seem to have strong influence on the star formation activity of the galaxies, in contradiction with the results found at low redshift (e.g. Ho 2005). For example, based on FIR data from the *Herschel* Space Observatory, Santini et al. (2012) reported evidence of an enhancement on the star formation activity in the host galaxies of a sample of X-ray-selected AGN at $0.5 < z < 2.5$, as compared to a mass-matched control sample of non-active galaxies. However, when they only considered star-forming galaxies in the control sample (i.e. they discarded quiescent galaxies), they found roughly the same level of star formation as in the AGN hosts. A similar result was found by Lutz et al. (2010), based on submillimetre data of a sample of 895 X-ray selected AGN at $z \sim 1$, for which they measured an SFR $\sim 30\,\mathrm{M_\odot\,yr^{-1}}$. This value, which they estimated assuming star formation-dominated submillimetre emission, is among the typical SFRs found for samples of non-active star-forming galaxies at $z \sim 1$ and $M_* \gtrsim 10^{10.5}\,\mathrm{M_\odot}$ (e.g. Noeske et al. 2007). Alonso-Herrero et al. (2008) studied the star formation properties of 58 X-ray-selected AGN at $0.5 < z < 1.4$ by modelling their multifrequency SEDs and did not find strong evidence for either highly suppressed or enhanced star formation when compared to a mass-matched sample of galaxies at the same redshift. However, these AGN were selected to have SEDs dominated by stellar emission, and thus, they are representative of only 50 per cent of the X-ray-selected AGN population.

In our previous work (Ramos Almeida et al. 2009; hereafter RA09), we fitted the optical to MIR SEDs of a sample of 116 X-ray-selected AGN in the Extended Groth Strip (EGS) with different starburst, AGN and galaxy templates from Polletta et al. (2007). Based on this SED fitting, we classified them as AGN-dominated (52 per cent) and host galaxy-dominated (48 per cent) objects. The latter have SEDs typical of starburst, spiral or elliptical galaxies, indicating the presence of a deeply buried or a low-luminosity AGN. From our SED fits, we derived photometric redshifts for all the galaxies, which range from $z_{\rm phot} = 0.05$ to 3. By dividing the sample according to the fitted templates, in RA09 we proposed an evolutionary sequence, similar to the one suggested for early-type galaxies by Schawinski et al. (2007): an intense period of star formation would be quenched by AGN feedback as the black hole (BH) accretes enough mass, competing for the cold gas reservoir and heating it, and becoming dominant. The AGN-phase would then continue through lower ionization phases, ending as spiral or elliptical galaxies hosting low-luminosity AGN.

This paper constitutes a spectroscopic follow-up of a representative subset of the AGN sample studied in RA09. These AGN were selected in the X-rays and all of them have MIR counterparts (i.e. detection in the 3.6, 4.5, 5.8, 8 and 24 μm bands of the *Spitzer Space Telescope*). See Section 2 for further details in the sample selection. Here, we present NIR spectroscopic observations for 28 of these AGN, which have spectroscopic redshifts in the range $z =$ [0.27, 1.28], and a median redshift of $z = 0.76$. These objects are representative of the whole sample in terms of redshift, magnitude and SED types (see Section 2), including 13 AGN-dominated and 15 host galaxy-dominated objects. The main goals of this work are first, to classify the galaxies spectroscopically to check the reliability of the SED classification done in RA09 and secondly, to obtain SFRs using the Hα emission. We will compare these SFRs with those obtained using *Spitzer* 24 μm observed fluxes. Throughout this paper, we assume a cosmology with $H_0 = 75\,\mathrm{km\,s^{-1}\,Mpc^{-1}}$, $\Omega_{\rm m} = 0.27$ and $\Omega_\Lambda = 0.73$.

2 SAMPLE AND PHOTOMETRIC DATA

The AGN sample studied in RA09 was originally selected by Barmby et al. (2006) in the X-rays, using *Chandra* data from Nandra et al. (2005) and *XMM–Newton* data from Waskett et al. (2004). Barmby et al. (2006) considered only the 152 X-ray sources lying within the boundaries of the *Spitzer* observations with a limiting full-band flux (0.5–10 keV) of $2 \times 10^{-15}\,\mathrm{erg\,s^{-1}\,cm^{-2}}$ in the case of the *XMM–Newton* data and of $3.5 \times 10^{-16}\,\mathrm{erg\,s^{-1}\,cm^{-2}}$ for the *Chandra* data. At the flux limits of these X-ray surveys, most of the sources are expected to be AGN and have $\log(f_{\rm X}/f_{\rm opt}) > -1$, indicating that they are not quiescent (i.e. non-active) galaxies. Finally, they selected the 138 objects with secure detections in the four *Spitzer*/IRAC bands (3.6, 4.5, 5.8 and 8 μm) and *Spitzer*/MIPS 24 μm band.

In addition to the X-ray and MIR data, in RA09 we used optical and NIR archival data from the AEGIS project[1] (Davis et al. 2007) to increase the coverage of the AGN SEDs. All the fluxes employed in RA09 were directly retrieved from the *Rainbow Cosmological Surveys data base*,[2] which is a compilation of photometric and spectroscopic data, jointly with value-added products such as photometric redshifts and synthetic rest-frame magnitudes, for several deep cosmological fields (Pérez-González et al. 2008; Barro et al. 2009, 2011). Of the 138 sources in the Barmby et al. (2006) sample, we discarded 42 galaxies that showed multiple detections in the ground-based images (optical and NIR) to avoid source confusion in the *Spitzer* MIR fluxes.

To classify the observed SEDs and estimate photometric redshifts, we combined optical data from the Canada–France–Hawaii Telescope Legacy Survey (*u*,*g*,*r*,*i*,*z*) T0003 worldwide release (Gwyn 2012); NIR fluxes (*J* and $K_{\rm S}$) from the version 3.3 of the Palomar-WIRC *K*-selected catalogue (Bundy et al. 2006) and *Spitzer* MIR data (IRAC 3.6, 4.5, 5.8 8 μm and MIPS 24 μm) from Barmby et al. (2006). We fitted these SEDs with the library of starburst, AGN and galaxy templates from Polletta et al. (2007) using the photometric redshift code HYPERZ (Bolzonella, Miralles & Pelló

[1] The AEGIS project is a collaborative effort to obtain both deep imaging covering all major wavebands from X-ray to radio and optical spectroscopy over a large area of sky. http://aegis.ucolick.org/index.html

[2] https://rainbowx.fis.ucm.es/Rainbow_Database

Table 1. Columns 1 and 2 list the ID from Barmby et al. (2006) and from the DEEP2 data base. Columns 3, 4 and 5 give the IRAC 3.6 μm right ascension and declination and the *J* mag from the Palomar-WIRC *K*-selected catalogue. For the galaxies lacking Palomar *J* mag values from the SED fits are given between brackets instead. Column 6 lists the observed hard X-ray luminosities from Nandra et al. (2005) and Waskett et al. (2004) in erg s^{-1}. Column 7 lists the spectroscopic redshift from DEEP2 when available (reliability is given between brackets: 3 = robust and 4 = very robust) and from other literature sources for the galaxies G17, G47 and G78. Columns 8 and 9 list the photometric redshift and the SED classification from RA09 (1 = SB-dom; 2 = SB-cont; 3 = Type-1; 4 = Type-2; 5 = NG). Refs: (a) Schneider et al. (2005); (b) Steidel et al. (2003) and (c) Lilly et al. (1995).

ID	ID DEEP2	RA (°)	Dec. (°)	*J* (AB)	log(L_X)	z_{spec}	z_{phot}	Group
G17	11039094	214.1768	52.3034	[17.41]	44.53	1.284 (a)	1.25	3
G25	11038472	214.2065	52.2815	[20.40]	42.97	0.761 (4)	0.75	5
G26	11038492	214.2079	52.3025	[20.27]	43.37	0.808 (4)	0.73	1
G27	11038266	214.2104	52.2763	[20.00]	43.45	0.683 (4)	0.60	2
G36	12004450	214.2675	52.4149	18.22	42.52	0.281 (4)	0.25	5
G43	12008608	214.2870	52.4525	18.87	42.08	0.532 (4)	0.47	5
G45	12008576	214.2940	52.4747	20.81	43.59	–	1.25	1
G47	12004491	214.2961	52.4280	18.44	≤41.79	0.418 (b)	0.34	5
G53	12004467	214.3134	52.4474	19.94	43.13	0.723 (4)	0.67	4
G55	12008051	214.3290	52.4623	[21.93]	≤43.03	1.211 (3)	1.23	1
G56	12008091	214.3303	52.4655	21.01	42.92	1.208 (3)	1.19	4
G57	12004011	214.3335	52.4168	21.77	42.71	–	0.70	4
G59	12012474	214.3456	52.5288	19.93	42.06	0.465 (4)	0.46	5
G60	12012471	214.3475	52.5316	20.14	42.68	0.484 (4)	0.50	4
G62	12012431	214.3510	52.5416	21.02	≤42.55	0.902 (4)	0.83	1
G63	12008225	214.3525	52.5069	18.84	43.31	0.482 (4)	0.54	3
G73	12012467	214.3859	52.5342	20.18	43.61	0.986 (4)	0.91	5
G74	12012543	214.3909	52.5637	19.95	42.70	0.551 (4)	0.52	5
G76	12012534	214.3932	52.5186	18.22	41.48	0.271 (4)	0.29	5
G78	12008222	214.3998	52.5083	18.93	44.66	0.985 (c)	1.04	3
G90	12007954	214.4244	52.4732	19.16	44.40	1.148 (4)	1.15	2
G91	12007926	214.4393	52.4976	20.25	43.33	0.873 (4)	0.87	1
G93	12007878	214.4415	52.5091	20.14	43.89	0.985 (3)	0.97	4
G99	12007962	214.4550	52.4676	20.13	42.88	0.996 (4)	1.00	5
G105	–	214.4657	52.5129	[22.10]	41.87	–	0.57	4
G106	12007949	214.4684	52.4814	[21.69]	43.22	–	1.00	4
G107	12007896	214.4707	52.4775	[20.10]	≤42.04	0.671 (3)	0.60	5
G110	12012132	214.4760	52.5232	[21.51]	42.56	–	0.65	4

2000). The templates span the wavelength range 0.1–1000 μm. See RA09 for a detailed description of the data, photometric redshift calculations and SED classification.

The galaxies were then classified in five main categories in terms of the template used to fit their SEDs.[3]

(i) *Starburst dominated*. Includes several templates of starburst galaxies (e.g. M82-like) and ultraluminous infrared galaxies (ULIRGs) with starburst (e.g. Arp 220 like).

(ii) *Starburst contaminated*. Comprises three different starburst composite SEDs: one starburst/Seyfert 1 and two starburst/Seyfert 2.

(iii) *Type-1*. Includes three Type-1 quasar (QSO) SEDs.

(iv) *Type-2*. Consists of two Type-2 QSOs, a Seyfert 2 and a Seyfert 1.8 SED.

(v) *Normal galaxy*. Includes the SEDs of three elliptical galaxies and seven spirals of different types.

Our main goal in RA09 was to classify the galaxies into these five groups and study their properties. It is worth clarifying that all of the sources are, in principle, AGN, on the basis of their X-ray and MIR emission, but only those included in the *Type-1*, *Type-2* and *Starburst-contaminated (SB-cont)* groups have AGN-dominated SEDs. On the other hand, those included in the *Starburst-dominated (SB-dom)* group have their SEDs dominated by starburst emission from the optical to the MIR. Finally, the *Normal galaxy (NG)* are weak AGN embedded in an otherwise elliptical or spiral galaxy emission.

It is possible, however, that a small fraction of the sample are star-forming galaxies emitting in the X-rays and MIR (see e.g. Pereira-Santaella et al. 2011; Ranalli et al. 2012). In order to confirm the dominance/presence of the AGN over the star formation/host galaxy emission and vice versa, and to estimate SFRs from the Hα emission, we obtained NIR spectroscopic data for a subsample of 28 galaxies (∼30 per cent of the total sample), which are representative of the five groups described above (see Table 1). In the following, we will refer to these 28 sources as AGN, although one of the goals of this work is to confirm the presence of nuclear activity.

In order to discard any possible bias in redshift and/or magnitude, in Fig. 1 we show histograms for the observed subsample and the whole RA09 sample. According to the Kolmogorov–Smirnov test, there is no significant difference between the two samples in terms of observed magnitude and redshift at the 2σ level.

In Fig. 2 we show the observed galaxy SEDs and the templates fitted in RA09 to classify them in the previously mentioned groups, as well as to estimate photometric redshifts. The fits are the same presented in RA09, with the exception of those of the

[3] http://www.iasf-milano.inaf.it/∼polletta/templates/swire_templates.html

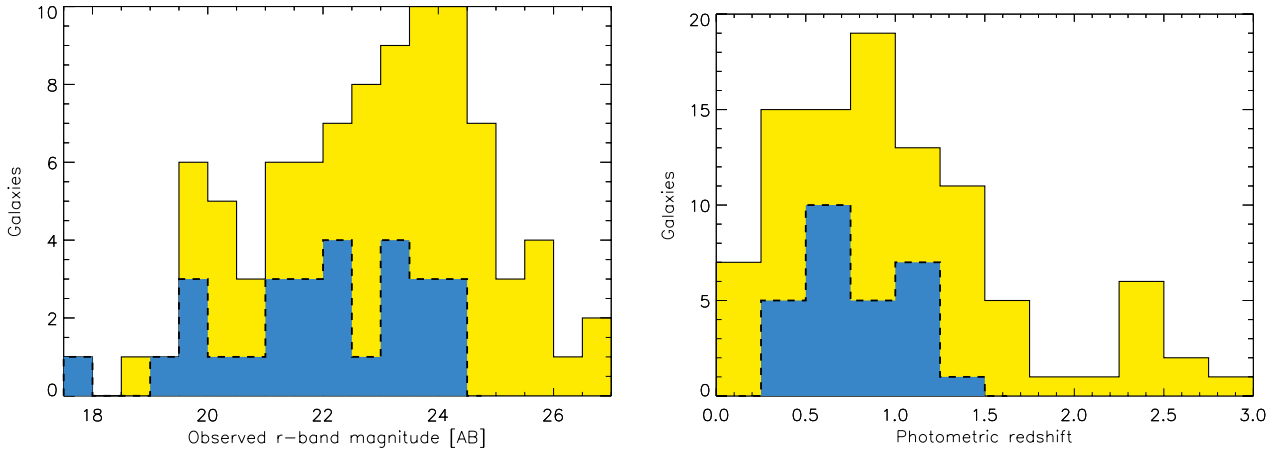

Figure 1. Left-hand panel: observed *r*-band magnitudes for the whole AGN sample studied in RA09 (yellow and continuous line histogram) and for the subsample of 28 galaxies observed with LIRIS (blue and dashed line histogram). Right-hand panel: same as in the left-hand panel, but for the photometric redshift distributions.

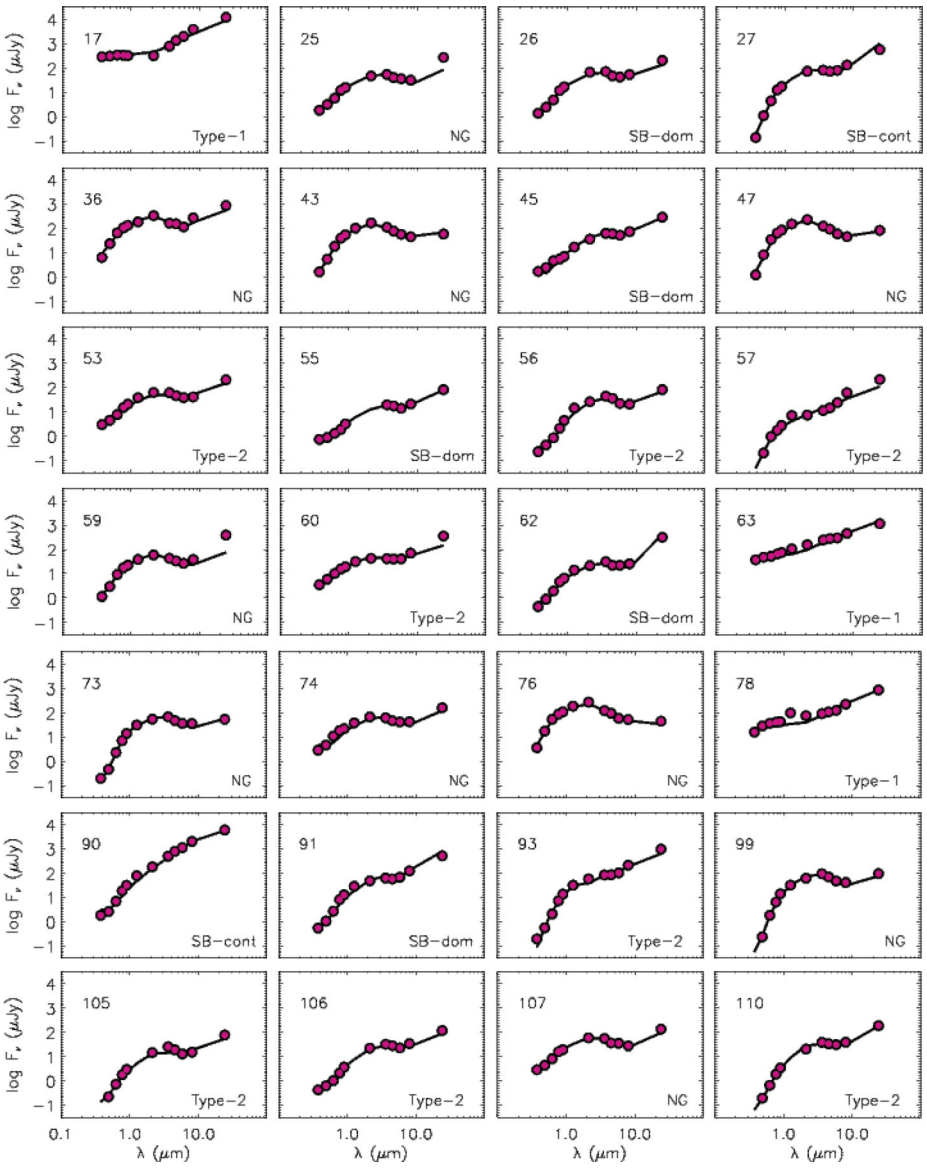

Figure 2. Observed SEDs (dots) of the subsample of 28 AGN observed with LIRIS, fitted with the AGN, starburst and composite templates from Polletta et al. (2007), using HYPERZ. The SED group and galaxy ID from RA09 are indicated in each panel.

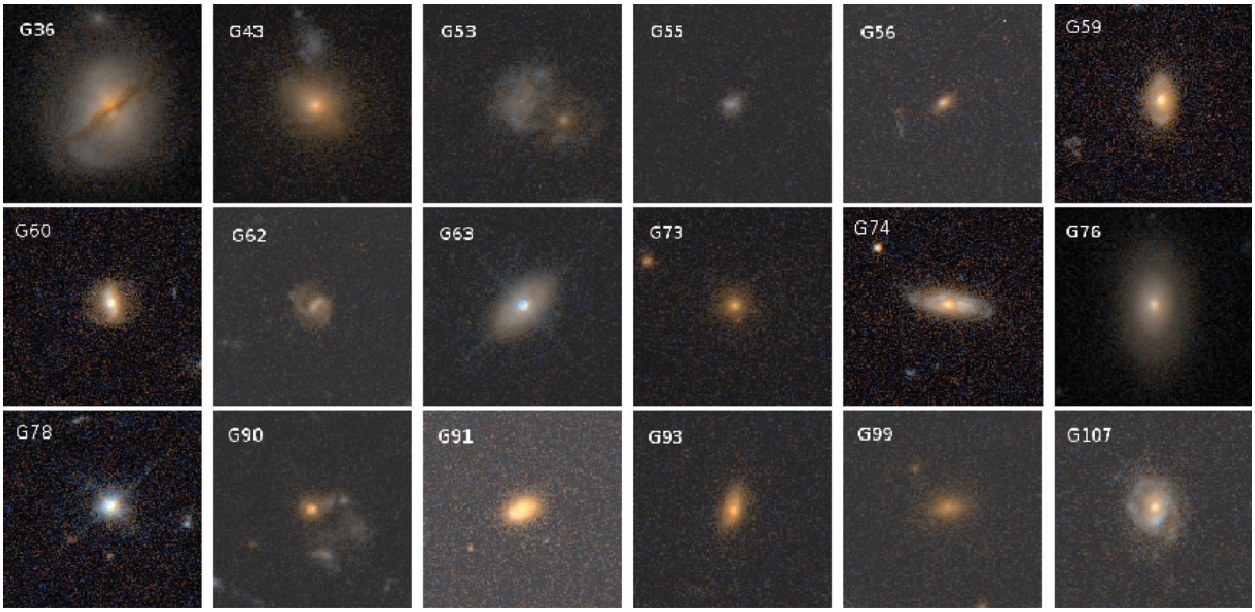

Figure 3. ACS/*HST* colour composite images of the 18 AGN in our LIRIS representative sample lying in the AEGIS ACS fields. Images are 7 arcsec in size and were downloaded from the AEGIS website (http://tkserver.keck.hawaii.edu/egs/egs.php). North is up and east is left.

Table 2. Summary of the NIR MOS observations.

Mask	Slits	Position	PA	Obs. date	Exposure time	Airmass	Seeing	Galaxies
EGS1	8	214.375, +52.535	5°	2008 March 28	4×6×600 s	1.09–1.35	∼1 arcsec	G59, G60, G62, G63, G73, G74, G76, G78
EGS2	8	214.293, +52.446	9°	2009 May 9	4×6×600 s	1.09–1.28	∼0.6 arcsec	G36, G43, G45, G47, G53, G55, G56, G57
EGS3	8	214.458, +52.498	26°	2009 May 8	4×6×600 s	1.09–1.41	∼0.7–0.9 arcsec	G90, G91, G93, G99, G105, G106, G107, G110
EGS5	4	214.182, +52.283	26°	2009 May 8, 9	2×6×600 s	1.55–1.98	∼0.6–0.7 arcsec	G17, G25, G26, G27

galaxies G17, G57, G78 and G105. We repeated these four fits because the photometric redshifts were not compatible with the spectroscopic redshifts derived from the NIR spectra presented here ($|\ z_{\rm NIR} - z_{\rm phot}\ | > 0.2$). We performed the fits using HYPERZ and restricting the input redshift range to $z_{\rm NIR} \pm 0.08$, which is the maximum difference between $z_{\rm NIR}$ and $z_{\rm phot}$ found for the rest of the sample observed with Long-slit Intermediate Resolution Infrared Spectrograph (LIRIS). This sample includes 5 *SB-dom*, 2 *SB-cont*, 3 *Type-1*, 8 *Type-2* and 10 *NG*, which were selected to cover the five SED groups and to maximize the number of targets in the LIRIS multislit masks (see Section 3.1).

Colour composite images obtained with the Advanced Camera for Surveys (ACS) on the *Hubble Space Telescope* (*HST*) for the 18 galaxies with data available in the AEGIS website[4] are shown in Fig. 3. The *Type-1* G63 and G78 show blue colours and strong point sources, while galaxies classified as either *Type-2* (e.g. G53) or *SB-dom* (e.g. G55 and G62) show obscured nuclei. Examples of spiral galaxies are G74 and G107, which were fitted with spiral templates in RA09. Finally, the morphology of G36 resembles that of an elliptical galaxy with a strong dust lane crossing the nucleus.

3 OBSERVATIONS AND DATA REDUCTION

3.1 NIR spectroscopy

NIR spectroscopic observations of the subsample of 28 galaxies selected from RA09 were obtained from 2008 March to 2009 May using the multi-object spectroscopic (MOS) mode of the NIR camera/spectrometer LIRIS (Manchado et al. 2004). LIRIS is attached to the Cassegrain focus of the 4.2 m WHT and it is equipped with a Rockwell Hawaii 1024×1024 HgCdTe array detector. The spatial scale is 0.25 arcsec pixel^{-1}.

Four masks were designed to observe a representative subset of the five groups described in Section 2. The galaxies were selected by their RA and Dec., to maximize the number of targets per mask. Details of each mask and the journal of observations are reported in Table 2. The chosen slit width was 0.85 arcsec, with the lengths varying between 8.5 and 12 arcsec, allowing enough space for nodding while avoiding overlap of the spectra. We used the low-resolution grism *ZJ*, which covers the range 0.8–1.4 μm, providing a spectral resolution of ∼500 km s^{-1} with the 0.85 arcsec slits. The spectral range varies depending on the position of the slits on the mask along the spectral direction. Thus, a slit in the centre of the mask will provide a spectrum in the nominal spectral range (0.8–1.4 μm), whereas spectra obtained with slits closer to the edges of the mask will be shifted either bluewards or redwards.

In addition to the science targets slitlets (see details in Table 2), each mask contained an extraslit, designed to simultaneously obtain the spectrum of a star of ∼16–17 mag in the *J* band (AB). These stars, which are brighter than the science targets (see Table 1), allowed, on the one hand, to ensure that the masks were well centred during the observation (the majority of the targets are too faint to be detected in single exposures), and on the other hand, to calculate the corresponding correction once the spectra were flux calibrated.

We performed the observations following an ABCABC telescope-nodding pattern, placing the source in three positions

[4] http://tkserver.keck.hawaii.edu/egs/

along the slit, using an offset of 3 arcsec around the central position of the pattern (B). Individual frames of 600 s in each nodding position were taken (see Table 2), amounting a total integration time of 3600 s per ABCABC pattern, and a total of 4 h per mask. Re-centring of the masks was done every hour, since the relative position between the star used for guiding and the science targets might have changed due to differential atmospheric refraction. The wavelength calibration was provided by observation of the argon lamp available in the calibration unit at the A&G box of the telescope. To obtain the telluric correction and the flux calibration for each galaxy, the nearby G0 stars HD 136674 and HD 115269 were observed before and after the science targets. Spectra of the two stars were obtained through three slitlets covering the whole wavelength coverage.

We reduced the data following standard procedures for NIR spectroscopy, using the LIRISDR[5] dedicated software within the IRAF[6] environment. For the MOS mode, the available routines use a priori mask design information to trace the slitlets positions and limits in a uniformly illuminated frame. We did not perform flat-field correction after checking that, at least in the case of our observations, it only introduced additional noise. We subtracted the mean of alternate pairs (A+C)/2 of two-dimensional spectra from that taken in the B position of the nodding pattern to remove the sky background. The resulting frames were wavelength calibrated before registering and co-adding all frames to provide the final spectra.

We then extracted the individual spectra for each galaxy and reference star, using an aperture of 1 arcsec, matching the maximum value of the seeing during the observations (see Table 2). We finally divided the extracted spectra by the corresponding G0 star spectrum to remove telluric contamination. We used a modified version of XTELLCOR (Vacca, Cushing & Rayner 2003) in this step, which provides both the telluric correction and the flux calibration.

We estimated the uncertainties in the galaxy fluxes due to slit losses for each mask using the reference stars, observed with the extraslitlet mentioned above. We finally corrected the fluxes of the science targets by applying a correction factor to the individual spectra. The observed NIR spectra of the 28 AGN are shown in Fig. 4–10. We have represented the observed *J*-band fluxes calculated from the Palomar-WIRC magnitudes reported in Table 1 for comparison with our flux-calibrated spectra. The Palomar fluxes were calculated in apertures of 2 arcsec diameter (Bundy et al. 2006) and thus correspond to total fluxes for the majority of the galaxies in the sample (see Fig. 3). Consequently, these *J*-band fluxes should be equal to or higher than the flux-calibrated LIRIS nuclear spectra, as indeed happens for all the galaxies. This gives us extraconfidence in our flux calibration. For those galaxies without Palomar *J*-band magnitudes available (see Table 1), values from the SED fits shown in Fig. 2 are given instead, and are represented as open diamonds.

The largest differences between the *J*-band photometry and spectroscopy are found for the galaxies G36, G43 and G47. The three of them are *NG* according to our SED fits, which are in agreement with their early-type morphologies, at least for G36 and G43 (those with ACS images available; see Fig. 3). Thus, the nuclear flux of these objects (the spectra were extracted using apertures of 1 arcsec) will not be the dominant contribution to the total flux, as opposed to the AGN-dominated galaxies. In addition, the three galaxies have relatively low redshifts: $z = [0.28, 0.53]$, making more different their nuclear and total emission. For example, 1 arcsec at $z = 0.3$ and 0.8 corresponds to 4.2 and 7.1 kpc, respectively.

3.2 DEEP optical spectroscopy

As indicated in Table 1, for 20 of the galaxies in the sample observed with LIRIS there are publicly available spectroscopic data from the Deep Extragalactic Evolutionary Probe 2 (DEEP2; Davis et al. 2003). The spectra were obtained during 80 nights between 2002 and 2005 using the *Deimos* multi-object spectrograph (Faber et al. 2003) on the Keck-II telescope, which provides a spectral resolution $R = \lambda/\Delta\lambda \sim 5000$ covering the nominal range 6400–9100 Å. DEEP2 employed a slit width of 1 arcsec, providing a spectral resolution of 1.4 Å and dispersion of 0.3 Å pixel^{-1} (Davis et al. 2007). The reduced and extracted spectra were retrieved from the Keck website[7] and they correspond to the Data Release 3 (DR3).[8] Note that the Data Release 4 has recently become public (Newman et al. 2012), but we have checked that there are no changes in the spectra of our galaxies. Thus, here we use the DR3 integrated spectra extracted along the locus of constant λ, following Horne (1986), and corrected for the effects of tilted slits.

The DEEP2 spectra are not flux calibrated and do not have the same spatial resolution as the LIRIS data. However, this can be solved by individually scaling the optical spectra to the averaged continuum flux of the overlapping (or bluest) NIR spectra. The flux-calibrated optical spectra of the galaxies G25, G26, G27 and G36 are presented in Appendix A. The complete set of optical spectra can be found in the online version of this paper. Our main interest in having optical spectra of our galaxies is to measure Hβ fluxes for those galaxies with Hα detected in the NIR, and thus determine individual values of the extinction to correct our Hα fluxes.

4 RESULTS

The NIR spectra of the sample observed with LIRIS show a wide variety of spectral features, including:

(i) prominent emission lines typical of AGN and/or star-forming galaxies (e.g. G17, G53, G55, G60, G78 and G90).

(ii) Hα detected in absorption (G43 and G76).

(iii) Very weak emission lines or featureless spectra (e.g. G36, G99 and G106).

(iv) Double-peaked emission lines corresponding to different kinematic components (G63).

After scaling the DEEP2 spectra to the flux-calibrated LIRIS data, we measured the fluxes of the emission lines. We fitted Gaussian profiles using the Starlink program DIPSO. The resulting emission line fluxes and full width at half-maximums (FWHMs) of Hα, [N II]λ6584 Å, Hβ and [O III]λλ4959,5007 Å are reported in Table 3. Same but for other detected transitions, such as [O I]λ6300 Å,

[5] http://www.iac.es/project/LIRIS.

[6] IRAF is distributed by the National Optical Astronomy Observatory, which is operated by the Association of Universities for the Research in Astronomy, Inc., under cooperative agreement with the National Science Foundation (http://iraf.noao.edu/).

[7] http://tkserver.keck.hawaii.edu/egs/

[8] http://deep.berkeley.edu/DR3/

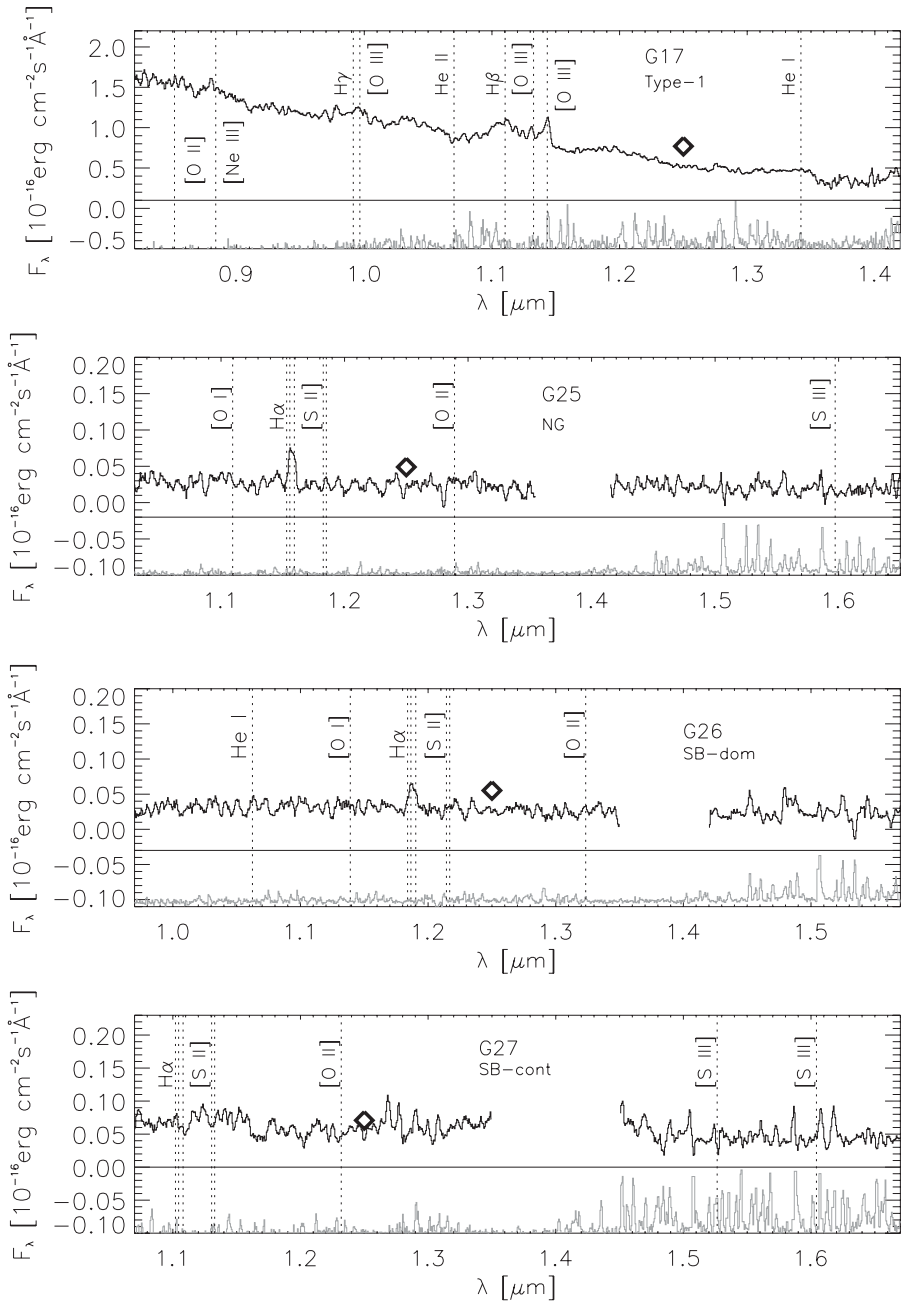

Figure 4. Observed NIR LIRIS spectra of the galaxies G17, G25, G26 and G27. Typical AGN emission lines are labelled. The Hα labels correspond to Hα+2[N II]. The SED classification from RA09 is indicated at the top of each panel, and an scaled sky spectrum for each galaxy is plotted at the bottom. Observed *J*-band fluxes from the magnitudes reported in Table 1 are represented with a cross for comparison. The open diamonds correspond to the *J*-band fluxes from the SED fits shown in Fig. 2.

[O II]λ3727,7320 Å, [O III]λ4363 Åand [S II]λ6732 Å are shown in Table 4. The line flux errors reported in Tables 3 and 4 are those given by DIPSO and they include the uncertainty associated with the fit. All the line fluxes reported correspond to detections at $\geq 1.5\sigma$ above the continuum noise, which we calculated as in Twite et al. (2012). We measure the continuum level and noise in two regions of ∼200 Å adjacent to a given emission line, and then calculate the $1.5 \times \sigma \times$ FWHM flux (hereafter 1.5σ) above the continuum. Emission line fluxes larger than that are quoted in Tables 3 and 4, otherwise we report an upper limit equal to the 1.5σ flux. The exception are the sources lacking a secure spectroscopic redshift (G45, G57, G105, G106 and G110), for which a larger detection significance of 2σ is required.

The majority of the emission lines are well reproduced with a single Gaussian of FWHM typical of the narrow-line region (NLR; $\lesssim$ 1000 km s^{-1}). For seven of the galaxies, namely G17, G55, G60, G63, G78, G90 and G107, an additional broad Gaussian component was needed to reproduce the observed line profiles of the permitted lines. The majority of these broad components have FWHM $\gtrsim$ 2000 km s^{-1}, typical of lines originated in the broad-line region. However, for some of the galaxies, intermediate-width components have been fitted instead (FWHM ∼ 1000–1500 km s^{-1}).

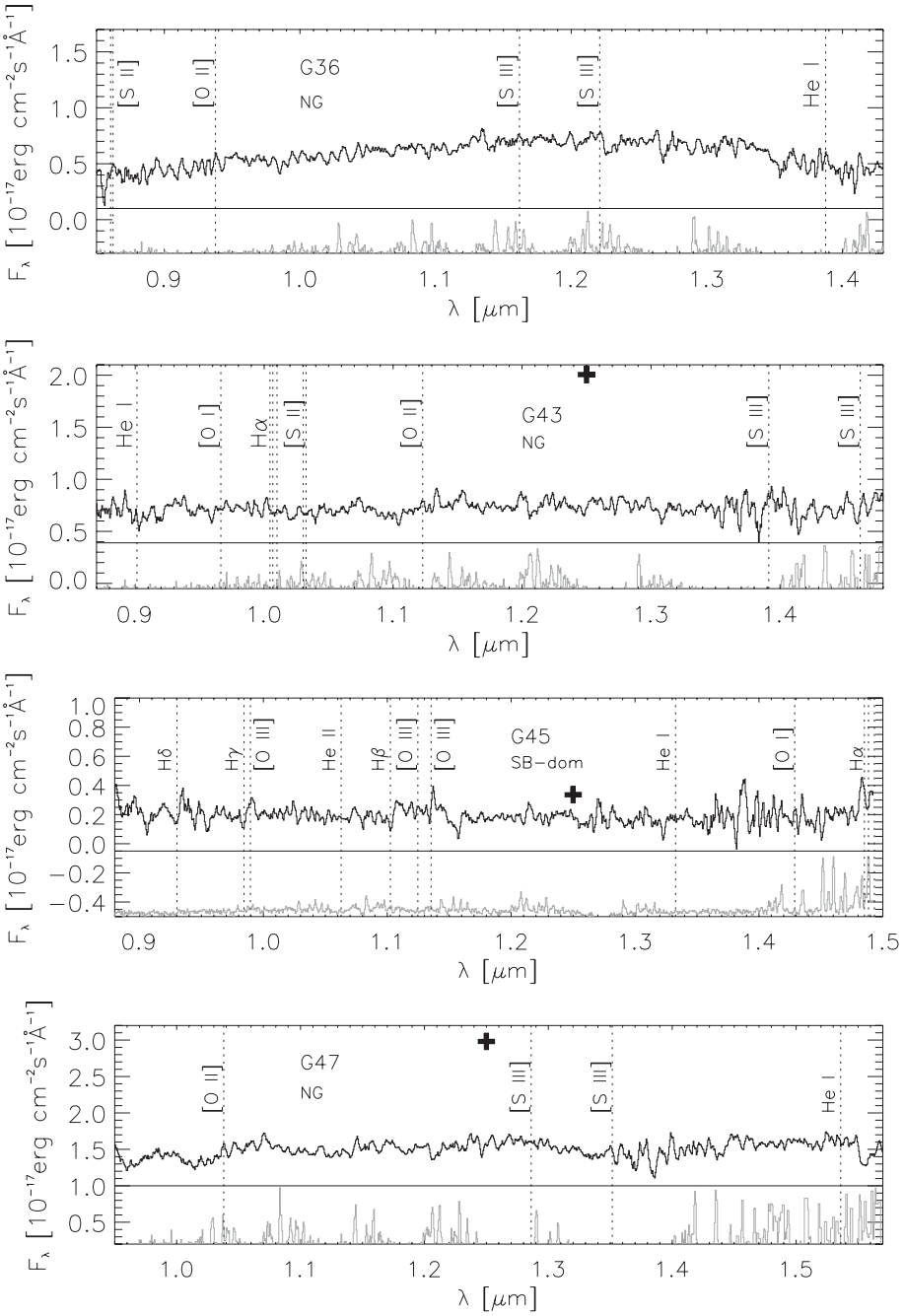

Figure 5. Same as in Fig. 4 but for the galaxies G36, G43, G45 and G47. The *J*-band flux of the galaxy G36 is out of scale (*J* flux = 3.65 × 10^{-17} erg cm^{-2} s^{-1} Å^{-1}).

Finally, in some cases it was necessary to fit two Gaussians to reproduce the profiles of the narrow lines in the DEEP2 spectra, of higher spectral resolution than the LIRIS data. This is the case of the galaxies G53, G55, G62, G63, G74, G93 and G99. In the LIRIS spectrum of G63, the double component of the Hα line is clearly resolved as well (see Fig. 7).

In Figs 4–10 we show a sky spectrum for each of the galaxies, extracted using the same aperture as for the nuclear spectra. Although the sky lines are removed from the spectra of the targets, as we described in Section 3.1, residual noise could be affecting the emission line fluxes reported in Tables 3 and 4. In particular, the galaxies whose Hα emission can be somehow affected by contamination of sky lines are G45, G55, G56, G90, G91, G93, G99 and G106.

4.1 Comparison between SED-fitting and spectral classification

On the basis of the spectroscopic features detected for the 28 galaxies observed with LIRIS, we can classify them spectroscopically to compare with the SED classification and to confirm the presence of nuclear activity. In Table 5, we summarize the results from this comparison.

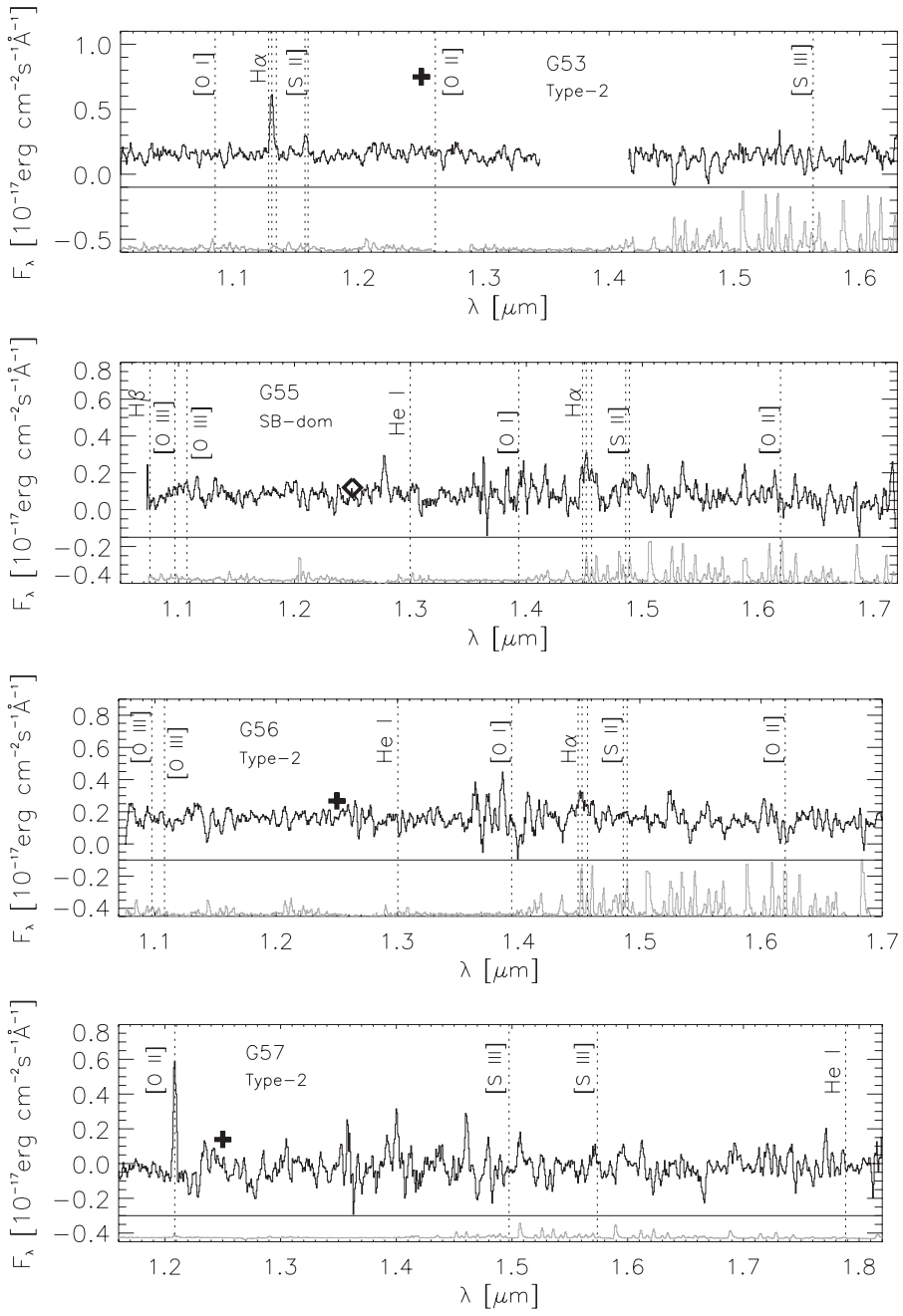

Figure 6. Same as in Fig. 4 but for the galaxies G53, G55, G56 and G57.

First, we have to confirm the presence of nuclear activity in all the sources. At the flux limits of the X-ray surveys from which the sources were selected, most of the galaxies are expected to be AGN and have $\log(f_X/f_{opt}) > -1$, indicating that they are not quiescent (i.e. non-active) galaxies. Thus, in RA09 we assumed that all the X-ray/MIR sources were AGN. However, it is also possible that some of them are simply star-forming galaxies emitting in the X-ray. Thus, considering that here we have spectroscopic information for 28 galaxies, in addition to the SED classification and X-ray luminosities, it is worth confirming that they are AGN.

The first thing to check is the hard X-ray luminosities. According to Ranalli et al. (2012), the criterion for a secure AGN origin of the X-ray luminosity is $L_X > 10^{42}(1+z)^{2.7}$ erg s$^{-1} = L_X^{AGN}$. However, this criterion is extremely restrictive, since it ignores the existence of low-luminosity AGN. As an example, in Pereira-Santaella et al. (2011) the authors studied the X-ray emission of a sample of 27 local luminous infrared galaxies (LIRGs) and found that the largest 2–10 keV luminosity was 2×10^{41} erg s^{-1}. Such L_X corresponds to a LIRG that is forming stars at a rate of 92 M$_\odot$ yr^{-1}. Only 8/28 sources have $L_X < L_X^{AGN}$, namely G43, G47, G55, G59, G62, G76, G105 and G107. Thus, for these galaxies, either their X-ray and MIR emission are due to intense star formation, or a heavily obscured AGN.

Secondly, we will contrast the previous information with the spectroscopic and SED classifications. The three galaxies fitted

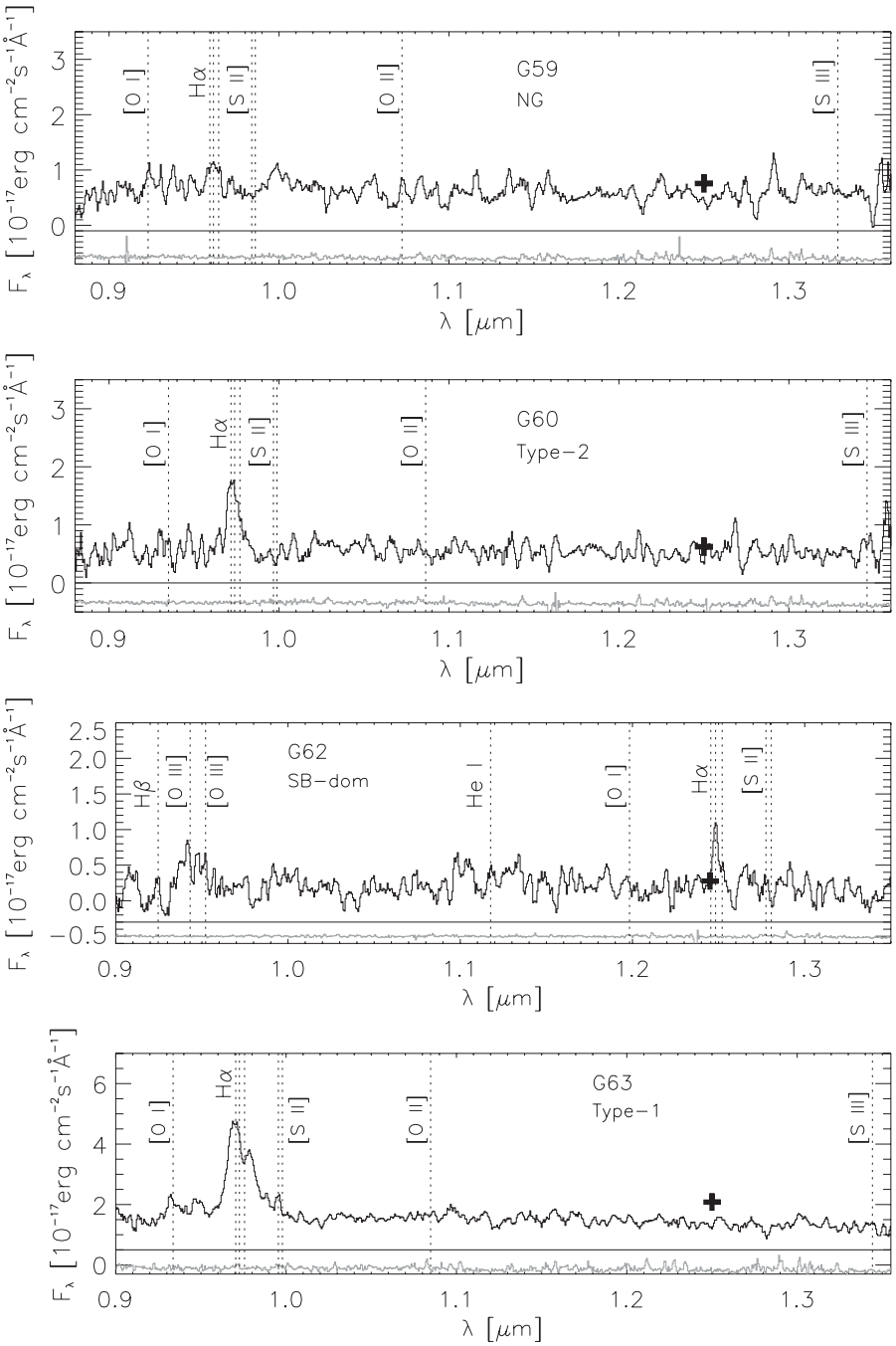

Figure 7. Same as in Fig. 4 but for the galaxies G59, G60, G62 and G63.

with *Type-1* templates (G17, G63 and G78; see Fig. 2) show broad components in their optical and/or NIR spectra. In fact, these are the only three galaxies with broad lines of FWHM > 3000 km s^{-1}. G90 shows broad Hα and Hβ components of FWHM $\sim$ 1800 km s^{-1}, in agreement with its SED classification as a *SB-cont*: the fitted template for this galaxy is a Sy1/starburst/ULIRG SED. On the other hand, there are another three galaxies with broad lines detected in their spectra (G55, G60 and G107) which were not classified as Type-1 AGN from their SED fits. Note, however, that those broad components have FWHMs $\lesssim$ 1500 km s^{-1}, and the luminosities of their broad Hα components are considerably lower than those of the galaxies G63, G78 and G90, as we show in Table 5. In fact, broad Hα emission is also detected in starburst galaxies (up to 2200 km s^{-1} in the case of stellar winds or supernovae remnants; see e.g. Boyle et al. 1995; Homeier & Gallagher 1999; Westmoquette, Smith & Gallagher 2011). Thus, G55 and G107 could be either normal galaxies with intense star formation or heavily obscured Type-1 AGN.

For G43 and G76 we detect Hα in absorption (as well as Hβ in the case of G43), which is characteristic of early-type galaxies. This agrees with our SED classification as *NG* (see Table 5) and shows how deeply buried – or possibly absent – these AGN are. Of the

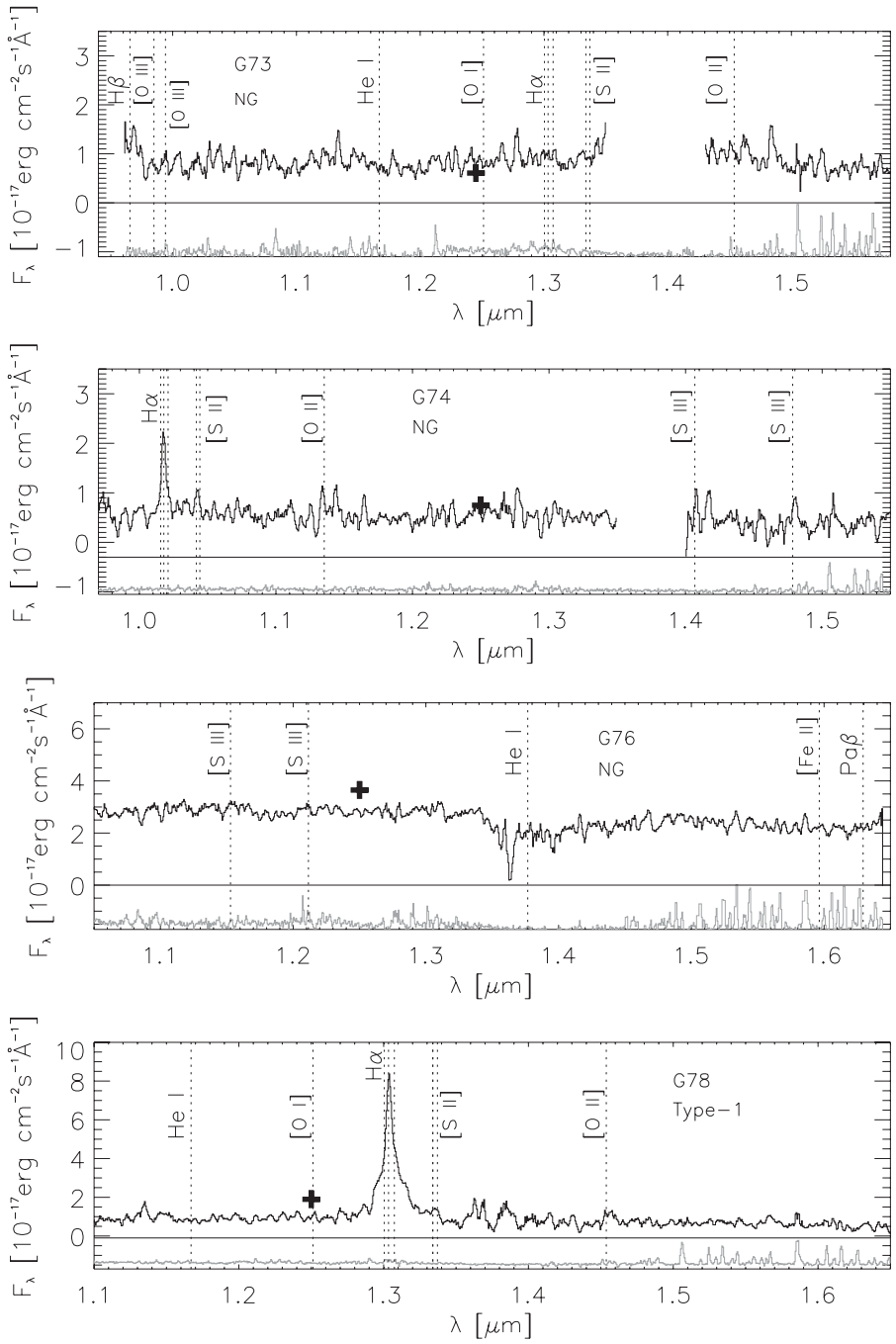

Figure 8. Same as in Fig. 4 but for the galaxies G73, G74, G76 and G78.

other galaxies classified in this group, some of them show narrow permitted lines (G25, G36, G59 and G74) and the rest have either very faint emission lines or practically featureless spectra (G47, G73 and G99).

The galaxies classified as *SB-dom* (G26, G45, G62 and G91) show very similar spectra, with relatively faint Hα emission and Hβ either in absorption or detected with very low signal-to-noise ratio (S/N). Finally, the galaxies fitted with *Type-2* templates show narrow emission lines (G53, G56, G57, G93, G105, G106 and G110), as well as the *SB-cont* G27, whose SED was fitted with a Seyfert 2/starburst template in RA09.

To definitely confirm the agreement between the SED and spectroscopic classifications, we have plotted the line fluxes reported in Table 3 in a Baldwin–Phillips–Terlevich (BPT) diagram (Baldwin, Phillips & Terlevich 1981). In Fig. 11 we show the [O III]λ5007/Hβ versus [N II]λ6584/Hα ratios for the 11 galaxies in our sample with the four emission lines involved detected. Despite the low number of galaxies represented in this BPT diagram, examples of the five SED groups are included. Note that we have considered only the fluxes of the narrow-line components in this figure. The empirical separations between AGN and H II regions (dashed line = Kewley et al. 2001; solid line = Kauffmann et al. 2003) are shown together with the

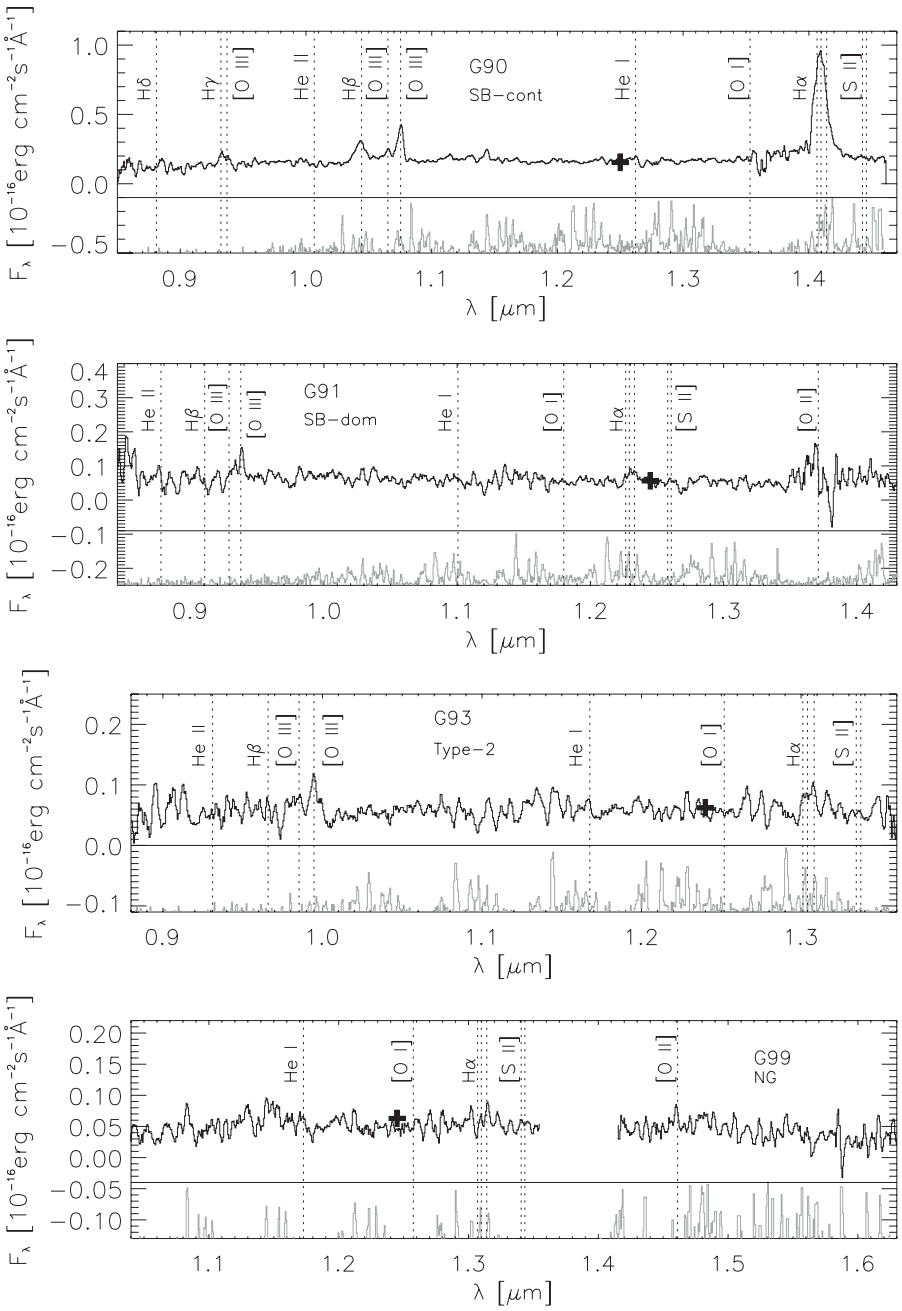

Figure 9. Same as in Fig. 4 but for the galaxies G90, G91, G93 and G99.

boundaries between low-ionization nuclear emission-line regions (LINERs) and Seyfert galaxies ([O III]/Hβ = 3 and [N II]/Hα = 0.6; Kewley et al. 2006).

As expected, the *Type-1* G63 and the *SB-cont* G90 are well above the H II region. The *Type-2*s G60 and G93 also lie in the AGN region of the diagram, but with ratios more typical of the Seyfert/LINER transition zone. G60 shows broad Hα and Hβ components in its spectrum, but appears much closer to the boundary between the H II and AGN regions than, for example, G63. The galaxy G107, which shows broad components in its recombination lines, although with FWHMs $\sim$ 900 km s^{-1} only, is located in the composite region between the Kauffmann et al. (2003) and Kewley et al. (2006) definitions. This agrees with our SED classification as an *NG* and with a possible star-forming origin of its X-ray luminosity (Pereira-Santaella et al. 2011; Ranalli et al. 2012), as discussed above. Thus, G107 might be either a very weak AGN whose optical/IR emission is diluted by the host galaxy, or a spiral galaxy with intense star formation (see Fig. 3 and table 1 in RA09).

Similar positions, also in the composite region, are occupied by the two *SB-dom* G26 and G62 and the *NG*s G25 and G74, confirming their SED classifications. Attending to their X-ray luminosities, only the galaxy G62 ($L_X \leq 42.55$ erg s^{-1}) could not be an AGN.

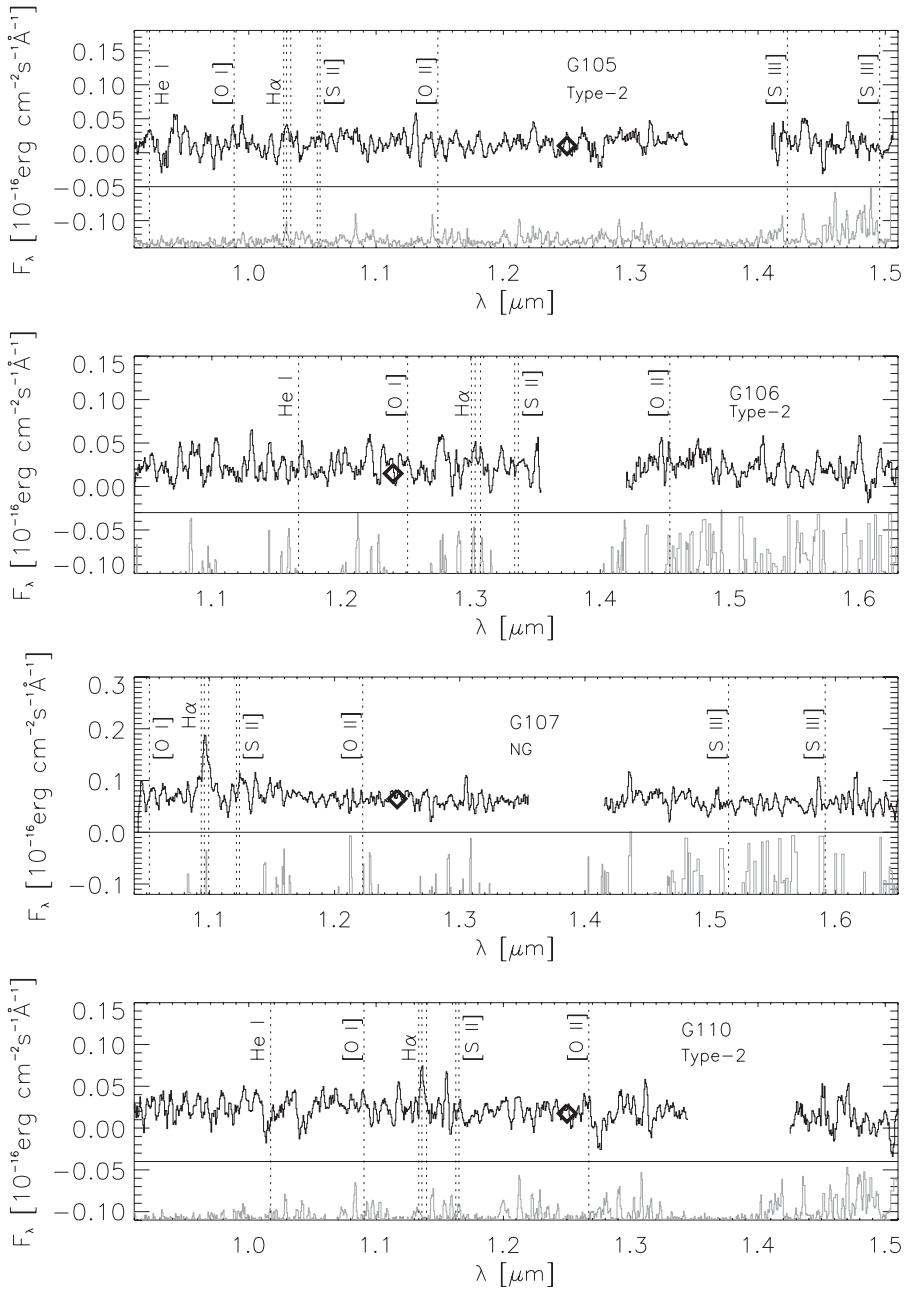

Figure 10. Same as in Fig. 4 but for the galaxies G105, G106, G107 and G110.

The position of the sources G53 and G59 in the BPT diagram is notable. We classified G53 as a *Type-2*, and its $L_{\rm X} > L_{\rm X}^{\rm AGN}$, but it is well below the H II boundary in the more restrictive Kewley et al. (2001) definition. This source is likely a weak AGN with intense star formation. On the other hand, G59, whose SED was fitted with a spiral template in RA09 and has $L_{\rm X} < L_{\rm X}^{\rm AGN}$, appears in the AGN region of the diagram, very close to the quasar G63. Thus, the galaxy G59 is likely a heavily obscured Type-2 AGN. In summary, according to the emission line fluxes represented in Fig. 11, our SED classification is correct for 9/11 galaxies.

Our previous work was aimed to distinguish between pure and host galaxy-dominated AGNs using SED fitting over a broad wavelength range. The use of accurate multiwavelength photometry, which is now available for several deep fields, to classify AGN, instead of spectroscopy, represents huge savings of both telescope time and data reduction effort. From the comparison presented here, we find that the SED classification method employed in RA09 works for 89 per cent of a representative sample of X-ray and MIR sources at $z \sim 0.8$ (see Table 5).

To further investigate the level of AGN dominance in these galaxies, in Fig. 12 we compare their observed hard X-ray fluxes (Waskett et al. 2004; Nandra et al. 2005) and 24 μm fluxes (Barmby et al. 2006) as in Alonso-Herrero et al. (2004). The area between dotted lines corresponds to the extrapolation of the median hard X-ray-to-MIR ratios ($\pm 1\sigma$) of local AGN ($z < 0.12$) selected in hard X-rays by Piccinotti et al. (1982). Same but for local starburst galaxies from Ranalli, Comastri & Setti (2003) is the region

Table 3. Line fluxes and FWHMs. Columns 2 and 3 list the spectroscopic redshifts from optical and NIR spectra, respectively. Column 4 corresponds to the line component that has been fitted (B: broad, N: narrow, Nb: blueshifted narrow and Nr: redshifted narrow component). Line fluxes ($\times 10^{-16}$ erg s^{-1} cm^{-2}) and FWHMs (km s^{-1}) of Hα, [N II]λ6584, Hβ and [O III]$\lambda\lambda$4959, 5007 are reported. The line flux errors reported are given by DIPSO, and they include the uncertainty associated with the fit. For several faint/undetected transitions, the continuum noise was used to calculate a 1.5σ upper limit to the line emission (those starting with :). For the sources lacking a secure spectroscopic redshift (G45, G57, G105, G106 and G110), a larger detection significance of 2σ is required. Brackets indicate that measurements are from DEEP2 optical spectra. Line widths have been corrected from instrumental broadening (18 and 3.6 Å for the LIRIS and DEEP2 spectra, respectively). Typical line width uncertainties are 25–30 per cent.

ID	z_{spec}		Comp.	Hα		[N II]λ6584		Hβ		[O III]λ4959		[O III]λ5007	
	z_{opt}	z_{NIR}		Flux	FWHM	Flux	FWHM	Flux	FWHM	Flux	FWHM	Flux	FWHM
17	1.284	1.284	N	–	–	–	–	1.06 ± 1.52	820	10.1 ± 1.9	810	21.2 ± 2.0	800
			B	–	–	–	–	55.7 ± 4.93	3400	–	–	–	–
25	0.761	0.761	N	1.48 ± 0.24	≤340	1.16 ± 0.21	≤340	[0.25 ± 0.02]	[140]	[:0.07]	[130]	[0.17 ± 0.02]	[130]
26	0.808	0.808	N	1.03 ± 0.33	≤280	0.72 ± 0.20	≤250	[0.09 ± 0.02]	[70]	[:0.05]	[70]	[0.10 ± 0.01]	[70]
27	0.683	–	N	:0.60	–	:0.60	–	[0.18 ± 0.04]	[50]	[0.29 ± 0.02]	[≤80]	[0.89 ± 0.05]	[≤80]
36	0.281	–	N	[0.66 ± 0.02]	[280]	[0.34 ± 0.01]	[280]	–	–	–	–	–	–
43	0.532	0.534	N	Abs	720	0.6 ± 0.3	720	[Abs]	[700]	[:0.08]	–	[:0.08]	–
45	–	1.268	N	:0.33	≤190	0.48 ± 0.13	≤190	Abs	≤180	:0.27	≤250	0.55 ± 0.13	≤250
47	0.418	0.418	N	–	–	–	–	–	–	–	–	–	–
53	0.723	0.722	Nb	1.47 ± 0.11	≤340	0.22 ± 0.09	≤340	[0.08 ± 0.01]	[≤75]	[:0.06]	[≤70]	[:0.06]	[≤70]
			Nr	–	–	–	–	[0.13 ± 0.02]	[≤75]	[:0.06]	[≤70]	[0.10 ± 0.01]	[≤70]
55	1.211	1.212	N	0.5 ± 0.2	≤180	0.27 ± 0.20	≤180	:0.23	–	:0.23	–	:0.23	–
			B	:2.02	1460	–	–	:1.65	–	–	–	–	–
56	1.208	1.213	N	0.88 ± 0.24	180	:0.33	180	:0.20	–	:0.20	–	:0.20	–
57	–	0.651	N	–	–	–	–	–	–	–	–	–	–
59	0.465	0.465	N	1.42 ± 0.50	230	1.05 ± 0.47	230	[0.32 ± 0.02]	[220]	[1.09 ± 0.03]	[210]	[3.46 ± 0.04]	[210]
60	0.484	0.484	N	1.14 ± 1.10	230	1.6 ± 0.6	230	[0.34 ± 0.02]	[170]	[0.30 ± 0.02]	[160]	[1.02 ± 0.03]	[160]
			B	6.09 ± 1.66	1510	–	–	[0.91 ± 0.08]	[1530]	–	–	–	–
62	0.902	0.902	N	2.87 ± 0.46	50	1.1 ± 0.4	50	:0.97	40	:0.97	40	1.67 ± 0.46	40
63	0.482	0.482	Nb	4.82 ± 0.98	590	4.67 ± 1.25	590	[0.07 ± 0.02]	[880]	[0.23 ± 0.03]	[850]	[0.69 ± 0.11]	[840]
			Nr	2.39 ± 0.68	230	1.33 ± 0.64	230	[0.10 ± 0.03]	[180]	[0.52 ± 0.03]	[310]	[1.57 ± 0.08]	[310]
			B	35.7 ± 4.0	5530	–	–	[12.7 ± 1.5]	[5880]	–	–	–	–
73	0.986	–	N	:0.79	–	:0.79	–	:1.13	–	:1.13	–	:1.13	–
74	0.551	0.551	Nb	5.25 ± 0.53	280	1.29 ± 0.44	280	[0.53 ± 0.07]	[120]	[0.40 ± 0.03]	[65]	[1.2 ± 0.1]	[65]
			Nr	–	–	–	–	[0.49 ± 0.07]	[120]	[0.36 ± 0.03]	[150]	[1.09 ± 0.08]	[150]
76	0.271	–	N	[Abs]	[210]	[0.9 ± 0.2]	[210]	–	–	–	–	–	–
78	0.985	0.986	N	17.97 ± 0.13	360	3.15 ± 1.56	410	–	–	–	–	–	–
			B	62.91 ± 0.34	3180	–	–	–	–	–	–	–	–
90	1.148	1.148	N	19.4 ± 3.2	640	16.4 ± 4.7	640	2.58 ± 1.33	780	4.78 ± 0.67	760	14.3 ± 0.8	750
			B	52.6 ± 8.9	1830	–	–	12 ± 2	1820	–	–	–	–
91	0.873	0.873	N	1.07 ± 0.27	≤260	1.07 ± 0.25	≤260	Abs	360	1.47 ± 0.38	350	2.61 ± 0.48	≤310
93	0.985	0.987	N	2.44 ± 0.83	130	3.58 ± 0.79	130	:0.81	120	:0.81	120	2.05 ± 0.47	120
99	0.996	0.996	N	:0.61	–	1.1 ± 0.3	–	–	–	–	–	–	–
105	–	0.569	N	1.01 ± 0.35	≤370	:0.68	≤370	–	–	–	–	–	–
106	–	0.986	N	:1.03	95	:1.03	95	–	–	–	–	–	–
107	0.671	0.670	N	2.6 ± 0.9	90	1.22 ± 0.57	90	[0.37 ± 0.07]	[≤90]	[:0.37]	[≤85]	[:0.37]	[≤85]
			B	2.05 ± 1.21	870	–	–	[:3.12]	[850]	–	–	–	–
110	–	0.731	N	1.74 ± 0.47	270	:0.69	270	–	–	–	–	–	–

between the dashed lines. The plot looks very similar to fig. 1 in Alonso-Herrero et al. (2004), where galaxies with redshifts in the range $z = 0.2$–1.6 were represented. Some of the AGN occupy the local AGN region and the rest lie in the transition zone between local starbursts and AGN. Of the 28 objects in Fig. 12, 18 are lying below the local AGN region (∼64 per cent), indicating either high absorption in the X-rays or intense star formation contributing to the 24 μm emission. Considering the relatively low values of the hydrogen column densities reported in Table 6 from Georgakakis et al. (2006), the first possibility is unlikely. We note, however, that the overall majority of the galaxies are very close to the local AGN region.

The position of the galaxies G17 and G90 in Fig. 12 is remarkable. They are the brightest 24 μm sources in the whole sample studied in Barmby et al. (2006)[9] and despite their strong Hβ and Hα broad components, they lie well below the AGN area of the diagram, indicating a strong contribution from star-heated dust at 24 μm.

It is also worth mentioning the position of the galaxies G53 and G59 in Fig. 12. Whereas G59 lies in the AGN region of the BPT diagram shown in Fig. 11, in Fig. 12 it appears considerably shifted from the local AGN region. Considering its low hydrogen column density ($N_H < 0.58 \times 10^{22}$ cm^{-2}; Georgakakis et al. 2006), the classification of this galaxy is unclear, although the BPT diagram confirms the presence of an active nucleus. Exactly the opposite

[9] 13.72 ± 0.01 and 14.51 ± 0.01 mag at 24 μm for G17 and G90, respectively.

Table 4. Same as in Table 3, but for other lines detected in the LIRIS and/or DEEP2 spectra.

ID	Comp.	Line	Flux	FWHM
36	N	[S II]λ6732	[0.17 ± 0.01]	[260]
43	N	[O II]λ7320	0.31 ± 0.17	530
45	N	Hγ	Abs	150
	N	[O III]λ4363	0.34 ± 0.10	≤280
47	N	[O II]λ7320	0.46 ± 0.14	220
53	N	[S II]λ6732	0.31 ± 0.30	≤340
55	Nb	[O II]λ3727	[0.09 ± 0.01]	[95]
	Nr		[0.10 ± 0.02]	[95]
56	N	[O II]λ3727	[0.17 ± 0.03]	[170]
57	N	[O II]λ7320	2.79 ± 0.24	180
59	N	[O II]λ7320	1.28 ± 0.40	210
62	Nb	[O II]λ3727	[0.24 ± 0.11]	[130]
	Nr		[0.50 ± 0.12]	[160]
63	N	[O I]λ6300	2.09 ± 0.97	470
74	N	[S II]λ6732	0.86 ± 0.32	270
90	N	[O II]λ3727	[1.63 ± 0.10]	[490]
91	N	[O II]λ3727	[0.59 ± 0.05]	[320]
93	Nb	[O II]λ3727	[0.14 ± 0.20]	[240]
	Nr		[0.51 ± 0.20]	[320]
99	N	[O II]λ7320	1.24 ± 0.54	170
	N	[S II]λ6732	:0.61	170
	Nb	[O II]λ3727	[0.2 ± 0.03]	[120]
	Nr		[0.2 ± 0.04]	[120]
110	N	[O I]λ6300	0.72 ± 0.41	280

happens to G53, which is definitely in the H II region of the BPT, but has typical MIR and hard X-ray AGN fluxes. In Table 5, we considered G53 and G59 as failures in the SED classification, but according to Fig. 12, it appears to be correct.

Summarizing, in view of all the discussed diagnostic diagrams, X-ray luminosities and SED classification, we cannot confirm the presence of nuclear activity in 4/28 sources (14 per cent of the sample): G47, G55, G62 and G107. These galaxies (1) have $L_{\rm X} < L_{\rm X}^{\rm AGN}$, (2) SEDs fitted with galaxy or starburst templates and (3) lie outside the AGN region in Figs 11 and 12. Note that they are the only four galaxies in the sample with upper limits for their X-ray luminosities (see Table 1). They could be low-luminosity AGN heavily obscured in the X-rays, but we cannot confirm it. Thus, in the following, we will exclude these four galaxies from the results found for AGN, although, for simplicity, we will refer to the whole sample of 28 galaxies as 'the AGN sample'.

4.2 SFR from Hα luminosity

By putting together the optical and NIR spectra of the galaxies, we have emission line flux measurements of Hα for 18/28 galaxies and upper limits for another five (see Table 3). In Table 6, we report the observed Hα luminosities ($L_{\rm H\alpha}$) obtained using the corresponding luminosity distances. In the absence of an AGN, the Hα luminosity is the best indicator of the instantaneous SFR, since Hα has little dependence on metallicity and it is much less affected by dust attenuation than the rest-frame UV continuum and Lyα (Kennicutt 1998; Bicker & Fritze-v. Alvensleben 2005).

In order to obtain SFRs for the galaxies in the sample using their Hα luminosities, we have to correct $L_{\rm H\alpha}$ from attenuation, using the A_V values reported in Table 6. We calculated them using the Hα and Hβ narrow-line fluxes, when available, and the standard Galactic extinction curve of Cardelli, Clayton & Mathis (1989) with $R_{\rm V} = 3.1$:

$$A_{\rm V}\,({\rm mag}) = 3.1 \times E(B-V) = 6.169 \times [\log({\rm H}\alpha/{\rm H}\beta) - 0.486].$$

Then, we obtained reddening values at the wavelength of emission of Hα ($A_{\rm H\alpha}$), and we used them to correct $L_{\rm H\alpha}$ from extinction. In Table 6, we report the attenuation-corrected Hα luminosities ($L_{\rm H\alpha}^{\rm corr}$) and corresponding errors.

The Hα emission in non-active galaxies is produced almost entirely by massive stars ($M > 10\,{\rm M}_{\odot}$), but in active galaxies it includes a contribution from gas photoionized by the AGN. In fact, this contribution will dominate in the case of pure AGN, and it will be, in principle, less important in the case of buried AGN. To test the latter, in Fig. 13 we represent $L_{\rm H\alpha}$ versus $L_{2-10\,{\rm keV}}$ from Waskett et al. (2004) and Nandra et al. (2005). Those X-ray luminosities are not absorption corrected, but considering the relatively low values of the hydrogen column densities reported in Table 6 from Georgakakis et al. (2006), we assume that they are not going to differ significantly from the intrinsic hard X-ray luminosities. The Hα luminosities plotted in Fig. 13 are not extinction corrected either, because we only have attenuation-corrected values for half of the sample (see Table 6).

If we consider the 2–10 keV luminosity as a proxy of the AGN, it should be correlated with $L_{\rm H\alpha}$ for AGN-dominated objects. Thus, we can derive an empirical relationship between $L_{\rm H\alpha}$ and $L_{\rm X}$ using the four galaxies that we can definitely classify as AGN-dominated from their spectra, SED fits and diagnostic diagrams presented in this work: G60, G63, G78 and G93. By fitting them, we find a correlation in the form $\log(L_{\rm H\alpha}^{\rm AGN}) = 0.95\,\log(L_{\rm X}) + 0.39$, with a correlation coefficient $r = 0.99$. G60 has a larger error bar than the other three pure AGN (see Fig. 13) because of the multicomponent fit performed to derive the Hα flux, in addition to its lower Hα emission as compared to that of G63, G78 and G93. However, in spite of its large error bar, G60 should be included in the AGN fit because it is the only pure-AGN representative of the lower luminosity objects in the sample. To ensure that we are not introducing any bias in the determination of $L_{\rm H\alpha}^{\rm AGN}$ by including G60, we performed the test of excluding it from the AGN fit, and we found $\log(L_{\rm H\alpha}^{\rm AGN}) = 0.87\,\log(L_{\rm X}) + 3.80$, with $r = 0.98$. The differences between the $L_{\rm H\alpha}^{\rm AGN}$ values derived from the two fits are much smaller than the $L_{\rm H\alpha}^{\rm SF}$ errors quoted in Table 6. Therefore, we can include G60 in the fit without introducing any bias in the final results.

Of the four pure AGN, G93 is the only one whose Hα flux could be marginally affected by sky line contamination. Looking carefully at the exact position of the sky lines, none of them coincides with λ(Hα), but the residuals of the sky subtraction could marginally affect the blue wing of Hα. To test how this could affect the determination of $L_{\rm H\alpha}^{\rm AGN}$, we repeated the same exercise as for G60, but excluding G93. In this case, we obtained $\log(L_{\rm H\alpha}^{\rm AGN}) = 0.97\,\log(L_{\rm X}) - 0.40$, with $r = 0.99$, which is even more similar to the original fit than when we excluded G60. Thus, including G93 makes no significant difference to $L_{\rm H\alpha}^{\rm AGN}$, and ultimately, to $L_{\rm H\alpha}^{\rm SF}$.

The luminosity of Hα will be partly due to the AGN and the star formation ($L_{\rm H\alpha} = L_{\rm H\alpha}^{\rm AGN} + L_{\rm H\alpha}^{\rm SF}$). If the 2–10 keV luminosity probes the AGN, objects lying above the correlation will have a significant contribution from star formation in their Hα emission (e.g. G56, G59, G62, G74, G105, G107 and G110). These galaxies have relatively low hard X-ray luminosities, indicating the presence of either a weak/absent AGN with intense star formation or a heavily

Table 5. Comparison between spectroscopic data and SED fitting. Column 2 corresponds to z_{spec} measured from the NIR and optical lines (see Table 3). In case of disagreement, we choose the most reliable value in terms of the S/N of the lines identified in each case. Columns 3, 4 and 5 indicate the emission line components fitted (B: broad, N: narrow, Nb: blueshifted narrow and Nr: redshifted narrow component) and the FWHM and luminosity of the broad component of Hα (Hβ in the case of G17), if present. Column 6 lists the SED-based classification of the galaxies as in RA09. Finally, columns 7 and 8 indicate whether or not there is agreement between the spectral and SED classifications, and if the presence of nuclear activity has been confirmed from the different diagnostic diagrams employed here.

ID	z_{spec}	Comp.	Hα broad		Group	Agreement	AGN
			FWHM (km s^{-1})	log L (erg s^{-1})			
17	1.284	N, B	3400 (Hβ)	43.69 (Hβ)	Type-1	$\surd$	$\surd$
25	0.761	N	–	–	NG	$\surd$	$\surd$
26	0.808	N	–	–	SB-dom	$\surd$	$\surd$
27	0.683	N	–	–	SB-cont	$\surd$	$\surd$
36	0.281	N	–	–	NG	$\surd$	$\surd$
43	0.532	N	–	–	NG	$\surd$	$\surd$
45	1.268	N	–	–	SB-dom	$\surd$	$\surd$
47	0.418	N	–	–	NG	$\surd$	?
53	0.723	Nb, Nr	–	–	Type-2	X	$\surd$
55	1.212	Nb, Nr, B	1500	$\leq$42.19	SB-dom	$\surd$	?
56	1.208	N	–	–	Type-2	$\surd$	$\surd$
57	0.651	N	–	–	Type-2	$\surd$	$\surd$
59	0.465	N	–	–	NG	X	$\surd$
60	0.484	N, B	1500	41.68	Type-2	X	$\surd$
62	0.902	Nb, Nr	–	–	SB-dom	$\surd$	?
63	0.482	Nb, Nr, B	5500	42.45	Type-1	$\surd$	$\surd$
73	0.986	N	–	–	NG	$\surd$	$\surd$
74	0.551	Nb, Nr	–	–	NG	$\surd$	$\surd$
76	0.271	N	–	–	NG	$\surd$	$\surd$
78	0.986	N, B	3200	43.46	Type-1	$\surd$	$\surd$
90	1.148	N, B	1800	43.55	SB-cont	$\surd$	$\surd$
91	0.873	N	–	–	SB-dom	$\surd$	$\surd$
93	0.987	N	–	–	Type-2	$\surd$	$\surd$
99	0.996	Nb, Nr	–	–	NG	$\surd$	$\surd$
105	0.569	N	–	–	Type-2	$\surd$	$\surd$
106	0.986	N	–	–	Type-2	$\surd$	$\surd$
107	0.670	N, B	900	41.55	NG	$\surd$	?
110	0.731	N	–	–	Type-2	$f\surd$	$\surd$

obscured AGN. At the high luminosity end, the *SB-cont* G90 shows an excess of Hα emission as well, explaining its position in Fig. 12. On the other hand, we have two galaxies lying below the correlation (e.g. G27 and G36). In the case of G36, high attenuation could be affecting its Hα emission, whereas in the case of G27 ($A_V \leq$ 0.23 mag) its Hα flux could be compromised by the line position, close to the edge of the detector (see Fig. 4).

Galaxies lying close to the AGN correlation shown in Fig. 13 will have $L_{H\alpha} \approx L_{H\alpha}^{AGN}$, whereas for those located well above, the $L_{H\alpha}^{SF}$ contribution to Hα will be significant. Thus, we use our AGN empirical correlation to calculate, for a given L_X, the expected $L_{H\alpha}^{AGN}$ of the galaxies. We then subtract this AGN contribution from the attenuation-corrected $L_{H\alpha}^{corr}$ values to obtain $L_{H\alpha}^{SF}$ (see Table 6). For the galaxies well below the correlation ($L_{H\alpha} \ll L_{H\alpha}^{AGN}$) we cannot estimate the AGN contribution to Hα even when $L_{H\alpha}$ has been extinction corrected, and thus we have used the total $L_{H\alpha}$ values as upper limits.

Ideally, this evaluation of the AGN contribution should have been done using attenuation-corrected Hα luminosities and intrinsic hard X-ray fluxes, since reddening in the optical and in the X-rays can be different (Fiore et al. 2012). However, we only have A_V values for nine galaxies and upper limits for another two. Besides, out of the four AGN-dominated sources that we use to derive the AGN correlation, only G60 has a reliable extinction value.[10] On the other hand, the observed and intrinsic hard X-ray luminosities will be similar, considering the low N_H values (Georgakakis et al. 2006). Thus, our method will be more reliable for galaxies with similar levels of obscuration in the optical and in the X-rays and vice versa.

We can now estimate SFRs for the galaxies in our sample using our individual $L_{H\alpha}^{SF}$ values and the Kennicutt (1998) conversion for Case B recombination at T_e = 10 000 K (Osterbrock 1989), assuming solar metallicity and a Kroupa & Weidner (2003) initial mass function (IMF):

$$SFR\ (M_\odot\ yr^{-1}) = 5.5 \times 10^{-42}\ L_{H\alpha}^{SF}\ (erg\ s^{-1}).$$

We obtain $SFR(L_{H\alpha}^{SF})$ = [0.03, 19] $M_\odot$ yr^{-1}, and two extreme values of 407 and 595 ($\pm$1000) $M_\odot$ yr^{-1} for the *Type-1*s G63 and G90, respectively. In the case of G63, it is likely that we have overestimated the extinction ($A_V = 7 \pm 2$ mag), because the fit of the Hβ profile using multiple components was particularly challenging. This galaxy does not appear to have such an intense star formation

[10] We have likely overestimated the A_V value for G63 ($A_V = 7 \pm 2$ mag). The fitting of its Hβ profile using multiple components was particularly difficult.

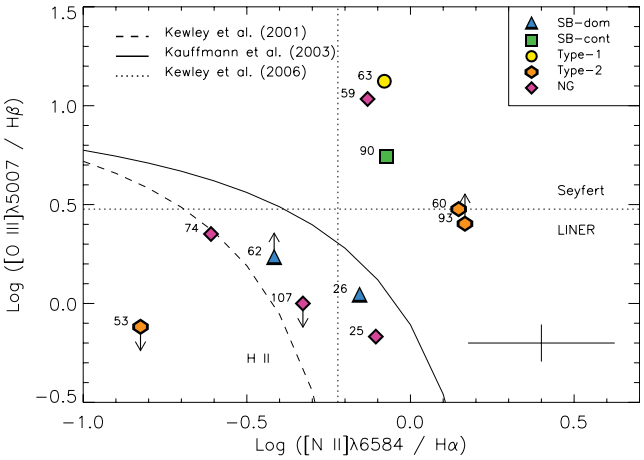

Figure 11. BPT diagram involving the emission-line flux ratios [O III]/Hβ and [N II]/Hα for the 11 galaxies in our sample with detections of the four emission lines involved. The empirical separations between AGN and H II regions, as defined in Kewley et al. (2001) and Kauffmann et al. (2003), are shown together with the boundaries between LINERs and Seyfert galaxies ([O III]/Hβ = 3 and [N II]/Hα = 0.6). The error bars at the bottom-right corner correspond to the typical uncertainties of the two ratios.

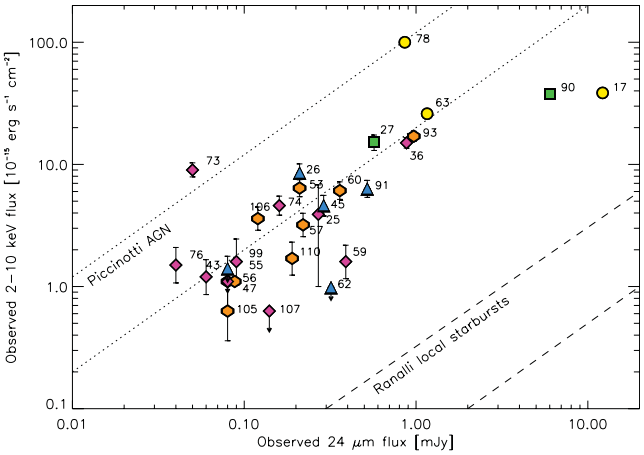

Figure 12. Observed 24 μm versus 2–10 keV fluxes. The areas between dotted and dashed lines correspond to the AGN region defined in Alonso-Herrero et al. (2004) from the Piccinotti et al. (1982) X-ray-selected AGN sample and to the local starburst region as defined in Ranalli et al. (2003), respectively. Symbols are the same as in Fig. 11. 24 μm flux errors are smaller than symbols (representative error is 0.01 mJy).

in Fig. 12, as opposed to G90. We will discuss the case of these two galaxies in Section 4.3.

The individual SFRs, with the exception of those of G63 and G90, are among the lowest reported in the literature for samples of non-active star-forming galaxies at similar redshifts and stellar masses (e.g. Twite et al. 2012; Rodríguez-Eugenio et al. in preparation), as we discuss in Section 5.

The average and median SFRs, measured using the values reported in Table 6, including upper and lower limits as fixed values, are 5 ± 5 and 2 $M_\odot$ yr^{-1}. We have excluded the extreme SFRs of G63 and G90 because of their large uncertainties, and those of G55, G62 and G107 because they are not confirmed AGN.

If we do not consider the upper and lower limits (i.e. if we only use the SFRs of the galaxies G25, G26, G53, G59, G60 and G74) the average and median SFRs are 7 ± 7 and 7 $M_\odot$ yr^{-1}. Note that none of these six galaxies has its Hα emission affected by sky line contamination.

4.3 SFR from observed 24 μm emission

In dusty galaxies, the UV light emitted by young stars is absorbed by dust and re-emitted in the IR. Therefore, the IR luminosity, either monochromatic or total, can be used to estimate the SFR (Kennicutt et al. 2009). In particular, the 24 μm luminosity is a good indicator of the current SFR of dusty star-forming galaxies (e.g. Alonso-Herrero et al. 2006; Calzetti et al. 2007; Rieke et al. 2009).

For galaxies whose Hα emission is obscured, both the AGN- and star-heated dust should be detected in the MIR. Thus, by comparing the Hα and 24 μm luminosities we can distinguish between galaxies with apparently low SFRs due to high levels of extinction and galaxies with negligible star formation. In Fig. 14, we compare the individual values of $L_{H\alpha}/L_X$ and L_{24}/L_X. The horizontal lines represent the mean AGN ratio in each case, using the four pure AGN G60, G63, G78 and G93. The galaxies G56, G59, G90, G105, G107 and G110 are well above the mean AGN ratios, indicating a strong contribution of star formation.

On the contrary, the *NG* G74, which in the left-hand panel of Fig. 14 is clearly above the AGN mean $L_{H\alpha}/L_X$, has a low L_{24}/L_X ratio. As discussed in Kennicutt et al. (2009), the galaxies with relatively low Hα luminosities ($L(H_\alpha) < 10^{42}$ erg s^{-1}) tend to have little dust, and consequently low A_V and weak IR emission. This could be the case of the galaxies G53 and G74.

The four galaxies for which we cannot confirm the presence of nuclear activity, G47, G55, G62 and G107, show large L_{24}/L_X values, indicative of warm dust emission produced by intense star formation and/or a heavily obscured AGN. The position of the galaxies G63 and G90 in the two panels of Fig. 14 confirms what we discussed in Section 4.2. G63 does not have a large L_{24}/L_X value as it is the case for G90. Thus, the extreme SFR measured from its Hα luminosity is likely the result of an overestimation of the A_V, whereas in the case of G90 it is probably real, although affected by a large uncertainty. In addition, G90 has its Hα emission somehow affected by sky line contamination.

The largest L_{24}/L_X value corresponds to the *Type-1* G17, for which we do not have an Hα measurement due to the galaxy redshift ($z = 1.28$). Finally, the *SB-dom* G45 and G91 show a MIR excess as compared to the Hα emission, indicative of relatively large A_V and in agreement with their SED classification as *SB-dom*.

To estimate SFRs using observed 24 μm emission, it is necessary to remove the contribution of AGN-heated dust from the total MIR emission, as we did for the Hα luminosities.

We have estimated the AGN contribution to the 24 μm emission of the individual galaxies using the SED fits shown in Fig. 2. For *Type-1* and *Type-2*, we have subtracted the 24 μm flux of the fitted template from the observed 24 μm flux. We assume that the flux difference corresponds to dust heated by star formation. The median AGN contributions are 97 per cent in the case of *Type-1* and 72 per cent for *Type-2* (see column 8 in Table 6). For the galaxies classified as *SB-dom* and *NG*, we consider that the 24 μm fluxes of the fitted templates are representative of the star formation, and any excess in the observed fluxes is due to the AGN (median AGN contribution of 4 per cent in the case of *SB-dom* and 25 per cent for *NG*). Finally, for the two *SB-cont*, we have repeated the SED fits using a *Type-2* template in the case of G27, and a *Type-1* template for G90, and consider the difference between the fitted and observed 24 μm fluxes as due to star-heated dust. The AGN contributions are 85 per cent for G27 and 91 per cent for G90.

Table 6. Observed, attenuation-corrected and AGN-corrected Hα luminosities calculated using the fluxes reported in Table 3 and the luminosity distances listed in column 2. The optical extinction listed in column 3 has been obtained from the observed Hα/Hβ ratios when available. Column 7 lists the SFRs obtained from $L^{\rm SF}_{\rm H\alpha}$. Column 8 corresponds to the observed 24 μm fluxes and the percentage of AGN contamination removed from the latter to calculate the IR SFRs reported in column 9, which have an accuracy of better than 0.2 dex; (Rieke et al. 2009). Columns 10, 11 and 12 indicate the 2–10 keV X-ray luminosities from Nandra et al. (2005) and Waskett et al. (2004), the column densities from Georgakakis et al. (2006) and the SED classification as in Table 1.

ID	Dist (Mpc)	$A_{\rm V}$ (mag)	$L_{\rm H\alpha} \times 10^{41}$ (erg s^{-1})	$L^{\rm corr}_{\rm H\alpha} \times 10^{41}$ (erg s^{-1})	$L^{\rm SF}_{\rm H\alpha} \times 10^{41}$ (erg s^{-1})	SFR ($L^{\rm SF}_{\rm H\alpha}$) (M$_\odot$ yr^{-1})	$F^{\rm obs}_{24}$ (mJy)	SFR ($F^{\rm SF}_{24}$) (M$_\odot$ yr^{-1})	$L_{\rm X} \times 10^{43}$ (erg s^{-1})	$N_{\rm H} \times 10^{22}$ (cm^{-2})	Group
17	8597	–	–	–	–	–	12.19 ± 0.11 (74 per cent)	>1000	33.9 ± 2.5	–	3
25	4481	1.77 ± 1.11	3.55 ± 0.58	13.3 ± 11.3	11.4 ± 11.3	6 ± 6	0.27 ± 0.01 (69 per cent)	8	0.93 ± 0.69	–	5
26	4823	3.53 ± 2.40	2.86 ± 0.92	40.0 ± 72.9	35.4 ± 72.9	19 ± 40	0.21 ± 0.01 (35 per cent)	17	2.35 ± 0.44	–	1
27	3916	≤0.23	≤1.10	≤1.10	≤1.10	≤0.6	0.57 ± 0.01 (85 per cent)	6	2.77 ± 0.40	–	2
36	1358	–	0.15 ± 0.01	≥0.15	–	–	0.88 ± 0.01 (36 per cent)	4	0.33 ± 0.03	8.82	5
43	2885	–	–	–	–	–	0.06 ± 0.01 (0 per cent)	2	0.12 ± 0.04	3.36	5
45	8449	–	≤2.82	–	–	–	0.29 ± 0.01 (5 per cent)	1000	3.91 ± 0.76	<0.08	1
47	2159	–	–	–	–	–	0.08 ± 0.01 (7 per cent)	1	≤0.06	<0.08	5
53	4203	2.21 ± 0.99	3.11 ± 0.23	16.2 ± 12.0	13.4 ± 12.0	7 ± 7	0.21 ± 0.01 (72 per cent)	4	1.35 ± 0.22	5.51	4
55	7990	–	3.82 ± 1.53	≥3.82	≥1.63	≥1	0.08 ± 0.01 (4 per cent)	77	≤1.06	<2.15	1
56	7963	≥0.97	6.67 ± 1.82	≥13.8	≥12.0	≥7	0.08 ± 0.01 (82 per cent)	4	0.83 ± 0.42	0.53	4
57	3681	–	–	–	–	–	0.22 ± 0.01 (51 per cent)	7	0.52 ± 0.11	0.33	4
59	2451	0.99 ± 2.21	1.02 ± 0.36	2.14 ± 3.61	1.88 ± 3.61	1 ± 2	0.39 ± 0.01 (81 per cent)	2	0.11 ± 0.04	<0.58	5
60	2571	0.24 ± 5.96	0.90 ± 0.87	1.08 ± 4.91	0.05 ± 4.92	0.03 ± 2.71	0.36 ± 0.01 (41 per cent)	7	0.48 ± 0.08	<0.24	4
62	5528	–	10.5 ± 1.7	≥10.5	≥9.72	≥5	0.32 ± 0.01 (0 per cent)	94	≤0.36	<5.84	1
63	2558	7.04 ± 2.30	5.64 ± 1.30	1084±1880	1080 ± 1880	595 ± 1034	1.16 ± 0.01 (100 per cent)	–	2.02 ± 0.15	<0.12	3
73	6179	–	≤3.61	–	–	–	0.05 ± 0.01 (0 per cent)	9	4.09 ± 0.55	0.72	5
74	3009	1.39 ± 1.05	5.68 ± 0.57	16.1 ± 12.7	15.0 ± 12.7	8 ± 7	0.16 ± 0.01 (25 per cent)	5	0.50 ± 0.09	2.16	5
76	1303	–	–	–	–	–	0.04 ± 0.01 (23 per cent)	0.1	0.03 ± 0.01	0.02	5
78	6171	–	81.8 ± 0.6	≥81.8	≥4.12	≥2	0.86 ± 0.01 (97 per cent)	3	45.3 ± 1.7	<0.04	3
90	7474	2.41 ± 3.34	130±21	784±1961	740 ± 1961	407 ± 1079	6.02 ± 0.05 (91 per cent)	>1000	25.3 ± 1.6	1.16	2
91	5307	–	3.60 ± 0.91	≥3.60	–	–	0.52 ± 0.01 (0 per cent)	163	2.11 ± 0.34	20.77	1
93	6173	–	11.1 ± 3.8	≥11.1	–	–	0.97 ± 0.01 (65 per cent)	166	7.71 ± 0.73	3.89	4
99	6262	–	≤2.86	–	–	–	0.09 ± 0.01 (20 per cent)	17	0.75 ± 0.33	3.63	5
105	3123	–	1.18 ± 0.41	≥1.18	≥1.01	≥0.6	0.08 ± 0.01 (69 per cent)	1	0.07 ± 0.04	2.25	4
106	6179	–	≤4.70	–	–	–	0.12 ± 0.01 (74 per cent)	4	1.64 ± 0.36	20.46	4
107	3830	2.22 ± 2.43	4.56 ± 1.58	23.9 ± 44.2	≥23.7	≥13	0.14 ± 0.01 (30 per cent)	7	≤0.11	<2.12	5
110	4250	–	3.76 ± 1.01	≥3.76	≥2.97	≥2	0.19 ± 0.01 (96 per cent)	0.2	0.37 ± 0.11	<0.26	4

We could have corrected the 24 μm fluxes from AGN contamination using the same technique employed in Section 4.2, but then we would have been left with no correction for those galaxies lying below the AGN mean ratio in Fig. 14.

Using the AGN-corrected 24 μm fluxes $F^{\rm SF}_{24}$ and equation 14 in Rieke et al. (2009):

$\log {\rm SFR}\ ({\rm M}_\odot\ {\rm yr}^{-1}) = A(z) + B(z)[\log(4\pi D_L^2 F^{\rm SF}_{24}) - 53]$,

we can calculate IR SFRs for the 28 galaxies in our sample (see Table 6). A(z) and B(z) are the SFR fit coefficients as a function of redshift for MIPS, and the above calibration assumes the Kroupa & Weidner (2003) IMF. We obtain values of SFR ($F^{\rm SF}_{24}$) = [0.1, 166] M$_\odot$ yr^{-1} and three extreme values of $\gtrsim$1000 M$_\odot$ yr^{-1} for the galaxies G17, G45 and G90. SFRs larger than 1000 M$_\odot$ yr^{-1} are only measured in ULIRGs and/or extreme starbursts (Magnelli et al. 2010). Given the position of G17 and G90 in Fig. 12 and in the right-hand panel of Fig. 14, the two galaxies must be ULIRGs. In fact, they both have monochromatic 24 μm luminosities larger than 45.5 erg s^{-1}, exclusive of this type of object (Alonso-Herrero 2007). The case of G45 is different. In the right-hand panel of Fig. 14 the galaxy does not show a strong excess in 24 μm over the AGN mean ratio. This indicates that we may have underestimated its AGN contribution to the 24 μm flux (only 5 per cent).

In general we find SFR ($F^{\rm SF}_{24}$) $\gtrsim$ SFR ($L^{\rm SF}_{\rm H\alpha}$), although for some galaxies SFR ($F^{\rm SF}_{24}$) < SFR ($L^{\rm SF}_{\rm H\alpha}$). This is expected, since the relation between Hα and 24 μm is non-linear, even when the Hα emission has been corrected from attenuation (see fig. 6 in Kennicutt et al. 2009). The average and median SFRs that we obtain from the 24 μm fluxes are 20 ± 50 and 5 M$_\odot$ yr^{-1}, respectively. We have excluded the extreme values of G17, G90 and G45 – which we do not consider representative of the sample – and those of the non-confirmed AGN. The median SFR is in agreement with that derived from the attenuation-corrected Hα luminosities. This similarity between the Hα and 24 μm median SFRs gives us extraconfidence in the AGN corrections that we have employed here.

5 COMPARISON WITH SAMPLES OF NON-ACTIVE GALAXIES

In Sections 4.2 and 4.3 we have estimated SFRs from attenuation- and AGN-corrected Hα luminosities and from AGN-corrected 24 μm fluxes. We obtain average SFRs = 7 ± 7 and 20 ± 50 M$_\odot$ yr^{-1}, respectively (median SFRs = 7 and 5 M$_\odot$ yr^{-1}). We now compare our SFRs with those published in the literature for different samples of non-active galaxies of similar stellar masses and redshifts, once converted to the Kroupa & Weidner (2003) IMF. The results of this comparison, including the conversion factors, when necessary, are summarized in Table 7. Although we do not know the individual stellar masses of our galaxies, the sample is representative of the X-ray selected population of AGN at $z \sim 0.8$, as we showed in Section 2, which typically have stellar masses in the range 0.8–1.2 × 10^{11} M$_\odot$ (e.g. Alonso-Herrero et al. 2008).

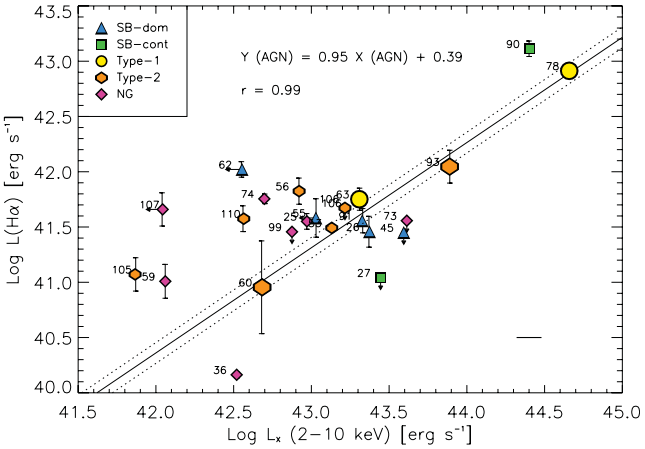

Figure 13. Hα versus hard X-ray luminosity (2–10 keV). The solid and dotted lines correspond to the AGN empirical relationship determined using the four AGN-dominated galaxies G60, G63, G78 and G93 (plotted with larger symbols) and 1σ limits, respectively. The correlation coefficient is $r = 0.99$. Objects well above this line are likely dominated by star formation, whereas those below may have Hα fluxes affected by extinction. L_X representative error is represented at the bottom-right corner.

We first compare with the small sample of seven star-forming galaxies selected by Doherty et al. (2004) from the Cohen et al. (2000) magnitude-limited sample ($R < 23$ mag) at $z \sim 0.8$. We used the Hα fluxes and reddening values reported in tables 1 and 2 in Doherty et al. (2004) to calculate attenuation-corrected SFRs exactly as we did for our AGN. We obtained SFRs = [4, 11] $M_\odot$ yr^{-1} for the individual galaxies and a mean of 7 ± 3 $M_\odot$ yr^{-1}, which is very similar to ours. Unfortunately, Doherty et al. (2004) did not give an indication of the stellar masses of their sample.

Secondly, Rodríguez-Eugenio et al. (in preparation) observed a sample of 30 star-forming galaxies at $z \sim 1$ and with $M_* \sim 10^{10.8}$ $M_\odot$ in the EGS with LIRIS MOS, for which there are DEEP2 optical spectra as well. They find an average SFR from aperture- and attenuation-corrected Hα luminosities of 23 ± 17 $M_\odot$ yr^{-1}, with individual values ranging from 5 to 64 $M_\odot$ yr^{-1}.

Twite et al. (2012) also used LIRIS MOS observations of galaxies at $z \sim 1$ and find attenuation-corrected values of SFR = [4, 319] $M_\odot$ yr^{-1}, with an average SFR of 66 ± 83 $M_\odot$ yr^{-1} for the 14 massive galaxies ($M_* > 10^{10.5}$ $M_\odot$) with extinction-corrected Hα measurements at the 1.5σ detection level.

Finally, based on Hα imaging of a sample of 153 star-forming galaxies at $z \sim 0.8$ with typical stellar masses of $\sim 10^{10}$ $M_\odot$, Villar et al. (2011) determined attenuation-corrected SFRs = [3, 23] $M_\odot$ yr^{-1}, with a median value of 8 $M_\odot$ yr^{-1}. This median SFR is very similar to ours (see Table 7). However, the average stellar mass of the Villar et al. (2011) sample is $\sim 10^{10}$ $M_\odot$, whereas the typical mass of AGN at $z \sim 0.8$ is $\sim 10^{11}$ $M_\odot$ (Alonso-Herrero et al. 2008). As represented in fig. 14 in Villar et al. (2011), the more massive the galaxies, the larger the SFRs (Dutton, van den Bosch & Dekel 2010; Villar et al. 2011). Thus, it is expected that the galaxies studied in Villar et al. (2011) have lower SFRs than those studied by Twite et al. (2012) and Rodríguez-Eugenio et al. (in preparation).

Again, in spite of the reduced size of the samples compared here, as well as the uncertainty affecting our AGN-corrected SFRs, the comparison presented might indicate that the presence of an AGN in a galaxy of $M_* \sim 10^{11}$ $M_\odot$ at $z \sim 0.8$, would be quenching its star formation. This quenching would be reducing the SFR from 20–50 $M_\odot$ yr^{-1} (typically found for samples of non-active star-forming galaxies at this redshift and stellar mass: Noeske et al. 2007; Twite et al. 2012; Rodríguez-Eugenio et al. in preparation) to less than 10 $M_\odot$ yr^{-1}. Alternatively, we might be seeing a delay between the offset of the star formation and AGN activity, as observed in the local Universe (Davies et al. 2007; Wild, Heckman & Charlot 2010).

6 COMPARISON WITH OTHER SAMPLES OF ACTIVE GALAXIES

Star formation activity in the hosts of AGN at intermediate redshift has been studied at longer wavelengths than those analysed here. For example, in a recent work based on FIR data from the *Herschel* Space Observatory, Santini et al. (2012) reported evidence of a higher average star formation activity in the hosts of X-ray selected AGN at $0.5 < z < 2.5$ compared to a mass-matched control sample of inactive galaxies. This enhancement is found to be higher for the most luminous AGN in the sample. However, when they only consider star-forming galaxies in the control sample, they found

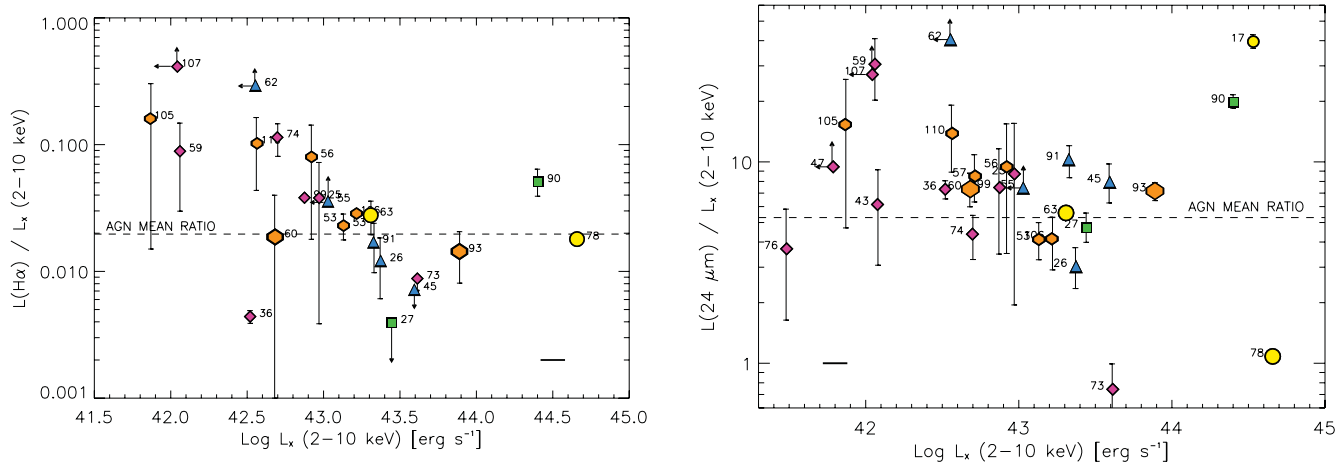

Figure 14. Left: $L_{H\alpha}/L_X$ versus hard X-ray luminosity (2–10 keV). Objects with a significant contribution of Hα due to star formation are clearly offset from the locus of galaxies. The horizontal dashed line corresponds to the mean value of $L_{H\alpha}/L_X$, considering the four pure AGN G60, G63, G78 and G93. Right: same as in the left-hand panel, but for L_{24}/L_X. L_X representative error is indicated at the bottom of the two panels.

Table 7. Comparison with SFRs (from Hα) of non-active star-forming galaxies from the literature. Columns 2 and 3 list the average/median redshift and an estimation of the stellar mass of the samples considered. In the case of our AGN sample, we considered a stellar mass of $\sim 10^{11}$ $M_\odot$, typical of AGN at this redshift (Alonso-Herrero et al. 2008). Columns 4, 5 and 6 give the intervals, average ($\pm$standard deviation) and median SFRs of the different samples, once converted to the Kroupa & Weidner (2003) IMF. Finally, column 7 lists the conversion factor applied to convert the SFRs to the Kroupa & Weidner (2003) IMF. Refs: (a) Salpeter (1955) and (b) Chabrier (2003).

Work	Redshift	M_* ($M_\odot$)	SFRs	Average SFR	Median SFR	IMF factor
Doherty et al. (2004)	$\sim$0.8	–	[4, 11]	7 ± 3	6	–
Rodríguez-Eugenio et al.	$\sim$1	$10^{10.8}$	[5, 64]	23 ± 17	19	0.696 (a)
Twite et al. (2012)	$\sim$1	$>10^{10.5}$	[4, 319]	66 ± 83	54	1.196 (b)
Villar et al. (2011)	$\sim$0.8	10^{10}	[3, 23]	–	8	0.696 (a)
This work	$\sim$0.8	$\sim 10^{11}$	[0.03, 19]	7 ± 7	7	–

roughly the same level of star formation activity in the hosts of AGN and non-active galaxies.

A similar result is reported by Lutz et al. (2010), but based on submillimetre data of a sample of 895 X-ray selected sources in the *Chandra* Deep Field South (CDFS) and extended CDFS. The latter authors analysed stacked emission at 870 μm, representative of X-ray-selected AGN at $z \sim 1$, and inferred an average SFR ~ 31 $M_\odot$ yr^{-1}, once converted to the Kroupa & Weidner (2003) IMF, and assuming star formation-dominated submillimetre emission. As claimed by Lutz et al. (2010), 30 $M_\odot$ yr^{-1} is among the typical values found for samples of non-active star-forming galaxies at $z \sim 1$ and $M_* \gtrsim 10^{10.5}$ $M_\odot$ (e.g. Noeske et al. 2007). In fact, this value is very similar to the average SFRs reported by Rodríguez-Eugenio et al. (in preparation) and Twite et al. (2012) for samples of star-forming galaxies at the same redshift and within the same range of stellar masses (see Table 7).

The star formation properties of 58 X-ray-selected AGN at $0.5 < z < 1.4$ were studied by Alonso-Herrero et al. (2008) by modelling their multifrequency SEDs. As in the previously mentioned works, they do not find strong evidence in the host galaxies of those AGN for either highly suppressed or enhanced star formation when compared to a mass-matched sample of galaxies at the same redshifts. However, these AGN were selected to have SEDs dominated by stellar emission, and thus, they are representatives of only 50 per cent of the X-ray-selected AGN population, and likely have higher SFRs than the other half of the population.

On the other hand, Bundy et al. (2008) studied the properties of the host galaxies of X-ray selected AGN at $0.4 < z < 1.4$ in the DEEP2/Palomar survey (Bundy et al. 2006), which includes the EGS, and found a different result. They estimated the star formation quenching rate, defined as the number of galaxies that move to the red sequence per Gyr. They found that this quenching rate coincided with the AGN triggering rate, assuming an AGN lifetime of $\sim$1 Gyr. Bundy et al. (2008) claimed that the agreement between the quenching and triggering rates may constitute evidence of a physical link between the two phenomena. However, the latter authors do not consider those X-ray selected AGN the cause of the quenching, but simply that they are somehow associated with it.

Thus, by putting together all the previous results, it seems that, for X-ray selected AGN, the period of moderately luminous AGN activity may not have strong influence in the star formation activity of the galaxies. In this context, our result would be against previous evidence for moderately luminous AGN not quenching star formation. However, the majority of these works are based on the assumption that the bulk of FIR and submillimetre emission is dominated by the host galaxy (see Mullaney et al. 2011, and references therein), and they are then used as a proxy of the star formation activity. Although this may be a valid assumption in general, other authors have identified the NLR clouds as the most likely location of the cool, FIR emitting dust (Dicken et al. 2009). In any case, such assumption has associated, to some degree, an overestimation the SFRs measured in AGN hosts.

An alternative scenario would be the existence of a time delay between the offset of the star formation and nuclear activity, as observed in the local Universe. Davies et al. (2007) analysed the star formation in the nuclear region of nine local Seyfert galaxies on scales of 10–100 pc and found evidence for recent, but not longer active, star formation. Sampling larger scales (up to 2 kpc radius) of SDSS selected starburst galaxies, Wild et al. (2010) found that the average rate of accretion of matter on to the BH rises steeply $\sim$250 Myr after the onset of the starburst. A similar result was found by Schawinski et al. (2009). More recently, Hopkins (2012) reported simulations of AGN fuelling by gravitational instabilities that naturally produce a delay between the peaks of SFR and nuclear activity. This offset scales as the gas consumption time and it is similar to those suggested by the observations on both small and large scales (Davies et al. 2007; Schawinski et al. 2009; Wild et al. 2010).

In order to confirm/discard the previous hypotheses, it is of extreme importance to perform accurate estimations of the AGN component to obtain reliable measurements of the SFRs in AGN hosts at $z \sim 1$ and beyond. In the future, we aim to repeat this study for a larger sample of AGN to derive statistically significant results. Considering the typical *J*-band magnitudes of AGN at redshift $z \sim 0.8$ ($\sim$20 mag), the use of 8/10 m telescopes is necessary to obtain higher S/N Hα detections. The new/upcoming NIR instruments FLAMINGOS-2 on the 8 m Gemini-South and EMIR (Espectrógrafo Multiobjeto InfraRrojo) on the 10 m Gran Telescopio Canarias (GTC) will represent a definitive leap in the study of intermediate-to-high redshift AGN.

7 CONCLUSIONS

We present new NIR spectroscopic observations of a representative sample of 28 X-ray and MIR selected sources in the EGS with a median redshift of $z \sim 0.8$ ($\Delta z = [0.3, 1.3]$). These galaxies show a wide variety of SED shapes, that we use to divide the sample in AGN dominated and host galaxy dominated. We combined LIRIS NIR spectra with DEEP2 optical spectroscopic data to maximize the number of Hα and Hβ detections. The main results from this study are summarized as follows.

(i) The NIR spectra (rest-frame optical) of the sample show a wide variety of spectral features, including prominent emission lines typical of AGN, Hα and Hβ in absorption, weak emission lines or featureless spectra, and emission lines with double kinematic components.

(ii) For 89 per cent of the sample, the spectroscopic and SED classifications are in agreement, confirming the reliability of multi-frequency SED fits to classify X-ray and MIR sources at intermediate redshift.

(iii) Using different diagnostics, we can confirm the presence of nuclear activity in 24/28 sources (86 per cent). The X-ray and MIR emission of the remaining four galaxies can be produced either by a heavily obscured low-luminosity AGN or intense star formation.

(iv) We estimate the AGN contribution to the observed 24 μm emission using the SED fits used to classify the galaxies: 97 per cent for *Type-1*, 72 per cent for *Type-2*, 88 per cent for *SB-cont*, 4 per cent for *SB-dom* and 25 per cent for *NG*.

(v) We calculate SFRs from attenuation and AGN-corrected Hα luminosities and obtain values within the interval SFR = [0.03, 19] $M_\odot$ yr^{-1}, which are in good agreement with the SFRs obtained from observed 24 μm fluxes: SFR = [0.1, 166] $M_\odot$ yr^{-1}. The average ($\pm$standard deviation) and median SFRs independently obtained from the two methods are (7 $\pm$ 7, 7) $M_\odot$ yr^{-1} and (20 $\pm$ 50, 5) $M_\odot$ yr^{-1}, respectively.

(vi) By comparing our results with those published in the literature for non-active star-forming galaxies of similar stellar masses and redshifts, we find that our SFRs are lower on average, although with a large dispersion. Despite the small size of the samples involved in this comparison, as well as the uncertainty affecting our AGN-corrected SFRs, the results provide an indication that the presence of an AGN in a galaxy at $z \sim 0.8$ might be quenching its star formation. Alternatively, we might be seeing a delay between the offset of the star formation and AGN activity, as observed in the local Universe.

ACKNOWLEDGMENTS

The authors acknowledge the Spanish Ministry of Science and Innovation (MICINN) through project Consolider-Ingenio 2010 Programme grant CSD2006-00070: First Science with the GTC (http://www.iac.es/consolider-ingenio-gtc/). CRA acknowledges the Estallidos group through project PN AYA2010-21887-C04.04 and STFC PDRA (ST/G001758/1). AAH acknowledges support from the Spanish Plan Nacional de Astronomía y Astrofísica under grant AYA2009-05705-E and from the Universidad de Cantabria through the Augusto González Linares Programme.

The authors acknowledge Kevin Schawinski, Roser Pelló, Carlos González Fernández, Omaira González Martín, Guillermo Barro, Andrew Cardwell, Berto González and Juan Carlos Guerra for their valuable help.

They also acknowledge the data analysis facilities provided by the Starlink Project, which is run by CCLRC on behalf of PPARC.

Based on observations made with the William Herschel Telescope operated on the island of La Palma by the Isaac Newton Group in the Spanish Observatorio del Roque de los Muchachos of the Instituto de Astrofísica de Canarias under the CAT programmes 18-WHT7/07B, 16-WHT7/08A, 26-WHT11/08B and 75-WHT23/09A.

Funding for the DEEP2 survey has been provided by NSF grants AST95-09298, AST-0071048, AST-0071198, AST-0507428 and AST-0507483 as well as NASA LTSA grant NNG04GC89G.

Some of the data presented herein were obtained at the W. M. Keck Observatory, which is operated as a scientific partnership among the California Institute of Technology, the University of California and the National Aeronautics and Space Administration. The Observatory was made possible by the generous financial support of the W. M. Keck Foundation. The DEEP2 team and Keck Observatory acknowledge the very significant cultural role and reverence that the summit of Mauna Kea has always had within the indigenous Hawaiian community and appreciate the opportunity to conduct observations from this mountain.

We finally acknowledge useful comments from the anonymous referee.

REFERENCES

Alonso-Herrero A., 2007, Rev. Mex. Astron. Astrofis. Conf. Ser., 29, 86
Alonso-Herrero A. et al., 2004, ApJS, 154, 155
Alonso-Herrero A. et al., 2006, ApJ, 640, 167
Alonso-Herrero A., Pérez-González P. G., Rieke G. H., Alexander D. M., Rigby J. R., Papovich C., Donley J. L., Rigopoulou D., 2008, ApJ, 677, 127
Baldwin J. A., Phillips M. M., Terlevich R., 1981, PASP, 93, 5
Barmby P. et al., 2006, ApJ, 642, 126
Barro G. et al., 2009, A&A, 494, 63
Barro G. et al., 2011, ApJS, 193, 13
Bicker J., Fritze -v., Alvensleben U., 2005, A&A, 443, L19
Bolzonella M., Miralles J.-M., Pelló R., 2000, A&A, 363, 476
Boyle B. J., McMahon R. G., Wilkes B. J., Elvis M., 1995, MNRAS, 276, 315
Brusa M. et al., 2009, A&A, 507, 1277
Bundy K. et al., 2006, ApJ, 651, 120
Bundy K. et al., 2008, ApJ, 681, 931
Calzetti D. et al., 2007, ApJ, 666, 870
Cardelli J. A., Clayton G. C., Mathis J. S., 1989, ApJ, 345, 245
Chabrier G., 2003, PASP, 115, 763
Cohen J. G., Hogg D. W., Blandford R., Cowie L. L., Hu E., Songaila A., Shopbell P., Richberg K., 2000, ApJ, 538, 29
Davies R. I., Müller Sánchez F., Genzel R., Tacconi L. J., Hicks E. K. S., Friedrich S., Sternberg A., 2007, ApJ, 671, 1388
Davis M. et al., 2003, Proc. SPIE, 4834, 161
Davis M. et al., 2007, ApJ, 660, 1
Dicken D. Tadhunter C., Axon D., Morganti R., Inskip K. J., Holt J., González Delgado R., Groves B., 2009, ApJ, 694, 268
Doherty M. et al., 2004, MNRAS, 354, L7
Dutton A. A., van den Bosch F. C., Dekel A., 2010, MNRAS, 405, 1690
Faber S. M. et al., 2003, Proc. SPIE, 4841, 1657
Ferrarese L., Merritt D., 2000, ApJ, 539, L9
Ferrarese L. et al., 2006, ApJ, 644, L21
Fiore F. et al., 2012, A&A, 537, 16
Gebhardt K. et al., 2000, ApJ, 539, L13
Georgakakis A. et al., 2006, MNRAS, 371, 221
Granato G. L., De Zotti G., Silva L., Bressan A., Danese L., 2004, ApJ, 600, 580
Greene J. E., Ho L. C., 2006, ApJ, 641, L21
Gwyn S. D. J., 2012, AJ, 143, 38
Ho L. C., 2005, ApJ, 629, 680
Homeier N. L., Gallagher J. S., 1999, ApJ, 522, 199
Hopkins P. F., 2012, MNRAS, 420, L8
Horne K., 1986, PASP, 98, 609
Kauffmann G. et al., 2003, MNRAS, 346, 1055
Kennicutt R. C., 1998, ARA&A, 36, 189
Kennicutt R. C. et al., 2009, ApJ, 703, 1672
Kewley L. J., Dopita M. A., Sutherland R. S., Heisler C. A., Trevena J., 2001, ApJ, 556, 121
Kewley L. J., Groves B., Kauffmann G., Heckman T., 2006, MNRAS, 372, 961

Kormendy J., Richstone D., 1995, ARA&A, 33, 581
Kroupa P., Weidner C., 2003, ApJ, 598, 1076
Lilly S. J., Hammer F., Le Fevre O., Crampton D., 1995, ApJ, 455, 75
Lutz D. et al., 2010, ApJ, 712, 1287
Magnelli B. et al., 2010, A&A, 518, L28
Magorrian J. et al., 1998, AJ, 115, 2285
Manchado A. et al., 2004, Proc. SPIE, 5492, 1094
Mullaney J. R., Alexander D. M., Goulding A. D., Hickox R. C., 2011, MNRAS, 414, 1082
Nandra K. et al., 2005, MNRAS, 356, 568
Newman J. A. et al., 2012, ApJS, preprint (arXiv:1203.3192)
Noeske K. G. et al., 2007, ApJ, 660, L43
Osterbrock D., 1989, Astrophysics of Gaseous Nebulae and Active Galactic Nuclei. University Science Books, Mill Valley, California
Pereira-Santaella M. et al., 2011, A&A, 535, 93
Pérez-González P. G., Trujillo I., Barro G., Gallego J., Zamorano J., Conselice C. J., 2008, ApJ, 687, 50
Piccinotti G., Mushotzky R. F., Boldt E. A., Holt S. S., Marshall F. E., Serlemitsos P. J., Shafer R. A., 1982, ApJ, 253, 485
Polletta M. et al., 2007, ApJ, 663, 81
Ramos Almeida C., Rodríguez Espinosa J. M., Barro G., Gallego J., Pérez-González P. G., 2009, AJ, 137, 179 (RA09)
Ranalli P., Comastri A., Setti G., 2003, A&A, 399, 39
Ranalli P. et al., 2012, A&A, 542, 16
Rieke G. H., Alonso-Herrero A., Weiner B. J., Pérez-González P. G., Blaylock M., Donley J. L., Marcillac D., 2009, ApJ, 692, 556
Rigby J. R., Rieke G. H., Donley J. L., Alonso-Herrero A., Pérez-González P. G., 2006, ApJ, 645, 115
Salpeter E. E., 1995, ApJ, 121, 161
Santini P. et al., 2012, A&A, 540, 109
Schawinski K. et al., 2007, MNRAS, 382, 1415
Schawinski K. et al., 2009, ApJ, 690, 1672
Schneider D. P. et al., 2005, AJ, 130, 367
Springel V., Di Matteo T., Hernquist L., 2005, MNRAS, 361, 776
Steidel C. C., Adelberger K. L., Shapley A. E., Pettini M., Dickinson M., Giavalisco M., 2003, ApJ, 592, 728
Trump J. R. et al., 2009, ApJ, 706, 797
Twite J. W., Conselice C. J., Buitrago F., Noeske K., Weiner B. J., Acosta-Pulido J. A., Bauer A. E., 2012, MNRAS, 420, 1061
Vacca W. D., Cushing M. C., Rayner J. T., 2003, PASP, 115, 389
Villar V., Gallego J., Pérez-González P. G., Barro G., Zamorano J., Noeske K., Koo D. C., 2011, ApJ, 740, 47
Waskett T. J., Eales S. A., Gear W. K., McCracken H. J., Brodwin M., Nandra K., Laird E. S., Lilly S., 2004, MNRAS, 350, 785
Wehner E. H., Harris W. E., 2006, ApJ, 644, L17
Westmoquette M. S., Smith L. J., Gallagher J. S., 2011, MNRAS, 414, 3719
Wild V., Heckman T., Charlot S., 2010, MNRAS, 405, 933

APPENDIX A: DEEP OPTICAL SPECTRA

Fig. A1 shows the optical spectra of four of the 20 galaxies in the sample with available data from DEEP2 (Davis et al. 2003). For details on how the observations were performed and other technical details, we refer the reader to Section 3.2. The flux calibration of these spectra was done by scaling them to the individual NIR LIRIS spectra. The 20 optical spectra available can be found in the online version of this paper.

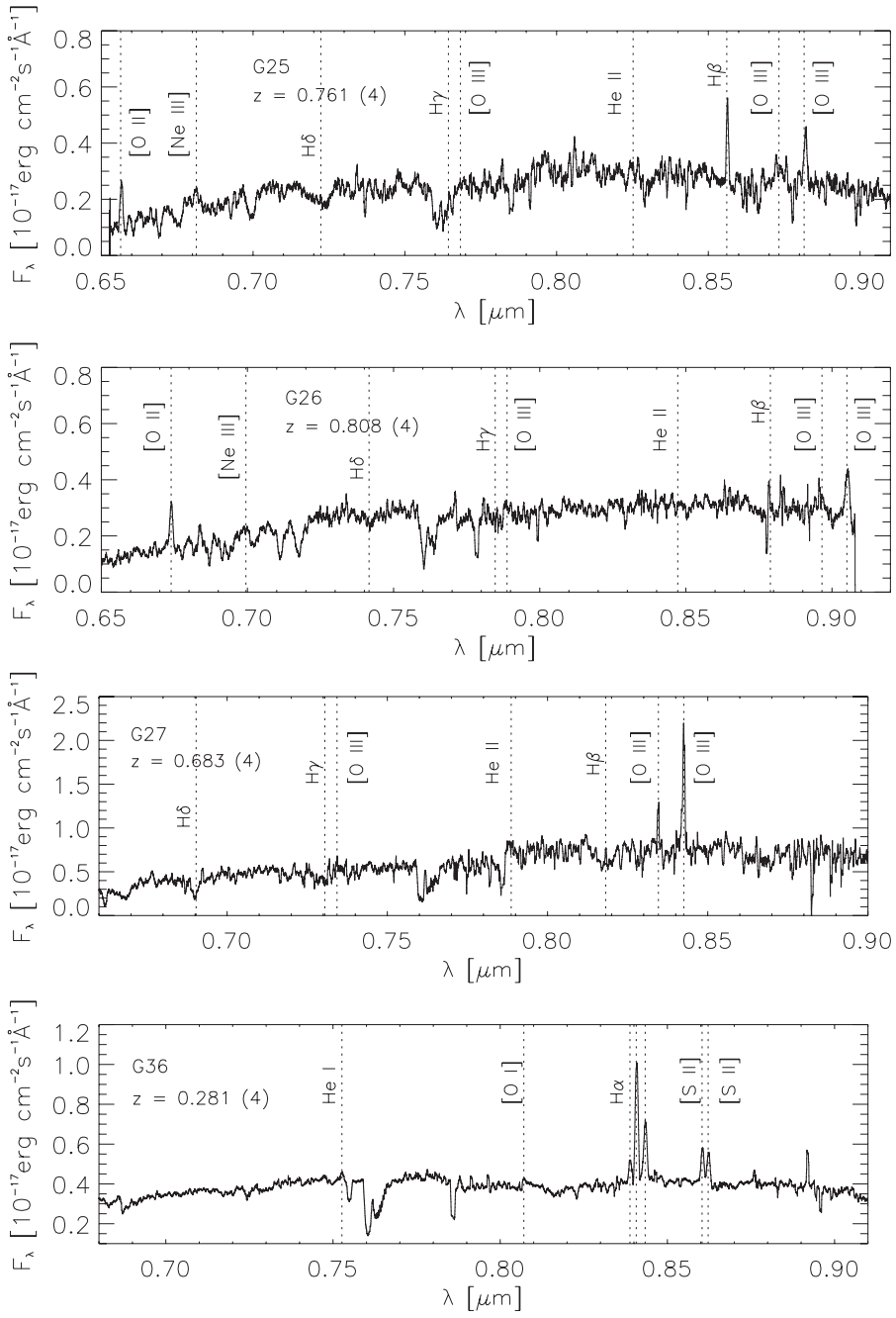

Figure A1. DEEP2 optical spectra of the galaxies G25, G26, G27 and G36. Typical AGN emission lines are labelled. The Hα labels correspond to Hα+2[N II]. The DEEP2 spectroscopic redshift is labelled in each panel, together with its reliability between brackets (1–2 = low and 3–4 = high reliability). The optical spectra of all the galaxies in the sample are available in the electronic version of the paper.

SUPPORTING INFORMATION

Additional Supporting Information may be found in the online version of this paper:

Figures A1 to A5 show the optical spectra of the 20 galaxies with DEEP2 data available (http://mnras.oxfordjournals.org/lookup/suppl/doi:10.1093/mnras/sts611/-/DC1).

Please note: Oxford University Press are not responsible for the content or functionality of any supporting materials supplied by the authors. Any queries (other than missing material) should be directed to the corresponding author for the article.

This paper has been typeset from a TEX/LATEX file prepared by the author.